**REVIEW**

# Recent advances in perovskite materials: exploring multifaceted properties for energy harvesting applications

Sahil Kumar[1] · Vishal Sharma[1] · Neha Kumari[1] · Gun Anit Kaur[1,2] · Anirban Saha[1] · Sapna Thakur[3] · Mamta Shandilya[1]

## Abstract

Perovskite materials have advanced significantly in the last several years, putting them at the forefront of research on energy harvesting, due to their remarkable piezoelectric, structural, electric, and optoelectronic properties. Enormous efforts have been made by various researchers to explore $ABO_3$ perovskite symmetry by playing with a variety of cations at the A and B sites. With an emphasis on the wide range of uses for perovskites in energy harvesting, this abstract offers a succinct summary of the most recent advancements in the field. Interestingly, perovskite solar cells have proven they can be widely used in the solar energy industry by reaching previously unheard-of levels of stability and efficiency. Perovskites are versatile and show their many uses outside of photovoltaics, such as in thermoelectric devices and light-emitting diodes. This article also explores the electronic and structural characteristics of perovskites that enable effective energy conversion. Their compositions can be adjusted to create materials with specific properties, leading to increased functionality and better performance. Herein, the crystal structure and intriguing properties of perovskite materials including dielectric, piezoelectric, ferroelectric, magneto resistance, and superconductivity have been discussed. Perovskite-based devices are also economically feasible choices for renewable energy technologies due to their low-cost manufacturing processes. It has been reported that perovskite materials are worthy materials for use in optoelectronic devices, transducers, ultrasonic devices, solid oxide fuel cells, ceramics, non-volatile memories, thin film capacitors, etc.

## Introduction

Solids with different surface morphologies are momentous in the era of smart material technology. The structure of the crystal was widely studied in the field of crystallography at the end of the nineteenth century, just before the advent of the atomic theory of solids. Gustav Rose first discovered the material called calcium titanium oxide ($CaTiO_3$) perovskite structure in the Ural Mountains of Russia in 1839. It was named after a Russian mineralogist, L.A. Perovski's name (1792–1856), and is widely known as one of the perovskite materials [1]. The term "perovskites" refers to both the structural classification and the mineral $CaTiO_3$. This dual usage of the term frequently causes confusion in the field of materials science, despite the fact that it is rarely explicitly addressed. In the textbook of Muller and Roy, they discussed about the nomenclature issue in depth and proposed a solution by introducing a formalization [2]. Therefore, $CaTiO_3$ represents the perovskite structure as opposed to the actual composition. Despite these efforts, the proposed formalization has not acquired widespread adoption, and confusion continues to exist [3]. The most common mineral in the planet Earth's crust is bridgmanite, which also adopts a perovskite structure. Ceramics are a special kind of material made from inorganic compounds of metal, metalloids held by ionic and covalent bonds. Some examples are quartz, mullite, calcium silicates, etc. Out of thousands of crystal structures, there are very few that dominate in ceramics. In these structures, $ABX_3$ perovskite is widely used because of its well-known electrical and piezoelectric properties. J. Curie and P. Curie in 1880 discovered that certain crystalline materials have the property of generating

✉ Mamta Shandilya
mamta2882@gmail.com

1   School of Physics and Materials Science, Shoolini University of Biotechnology and Management Sciences, Solan 173229, India

2   Institute of Advanced Materials, IAAM, Gammalkilsvägen 18, 590 53 Ulrika, Sweden

3   Department of Biotechnology, Akal College of Agriculture, Eternal University, Baru Sahib 173101, India

an electric charge when mechanical stress is applied, which is known as the piezoelectric effect [4, 5]. In 1948, a single crystal of $BaTiO_3$ was developed, and people studied the structure with the X-ray diffraction technique, polarization, and their dielectric response. It was possible to observe the domains and the change in their size, numbers, or orientation in the ferroelectric state. It was also observed that the displacement of the domain walls occurred with both polarized and non-polarized light. The Curie point was observed near 120 °C, along with two polymorphic transitions near 5 °C and $-70$ °C [6, 7]. A single crystal has a three-dimensional structure with repeated unit cell structures in all directions and a continuous structure throughout the crystal. Some examples of perovskite single crystals are $BaTiO_3$, $MgSiO_3$, etc. In 1921, Valasek observed the ferroelectric phenomenon and discovered the effect of the applied electric field in the opposite direction of the polarization within the Rochelle salt (potassium and/or sodium tartrate). In 1940, only two varieties of ferroelectrics were known: Rochelle salt and potassium dihydrogen phosphate, as well as their isomorphous counterparts [8, 9]. In 1950, with the discovery of $Pb[Zr_xTi1-x]O_3$ (PZT) and $BaTiO_3$ (BT), there was a remarkable growth in the research area of ceramics [10–14]. Later, in 1950, researchers tried to study the effect of the hydrostatic pressure on the $BaTiO_3$ single crystals. They had shown that with the increase in pressure, a linear shift of the Curie temperature towards lower temperature occurred, with a slope of $-5.8 \times 10^{-3}$ degrees per atom. This information was helpful in calculating the specific heat and compressibility at the Curie point. Hence, it was possible to relate changes in lattice constant due to the pressure effect [15]. Perovskite materials come in various categories, like ferroelectric [16], pyroelectric [17], piezoelectric, or dielectric. Moreover, some of the perovskite materials also exhibit superconductivity [18]. At room temperature, tetragonal $BaTiO_3$ is a ferroelectric perovskite ($ABO_3$). It is used as a dielectric in multilayer capacitors (MLCs) and as an overload safety device in electrical products. For MLC uses, the dielectric materials must have high electrical insulation ($> 10^{10}$) and high permittivity values ($> 1000$) at room temperature. When heated above the ferroelectric to paraelectric (tetragonal to cubic) phase transition temperature, overload protection devices should be semiconducting ($< 100\ \Omega$) and undergo a sharp rise in resistivity. In one of the most recent studies of ferroelectric ceramics, researchers have looked into a complicated perovskite structure with the chemical formula $(_{0.95-x})BiScO_3\text{-}xPbTiO_3\text{-}_{0.05}Pb(Sn_{1/3}Nb_{2/3})O_3$. This particular ceramic has a high Curie temperature ($T_C$) of 408 °C and a stable piezoelectric response at 200 °C, with a significant piezoelectric signal $d_{33}{}^* \approx 2500$ pm $V^{-1}$, which is the same as the expensive piezoelectric single crystals

that are built on relaxor materials at room temperature. In addition, at room temperature, it has a piezoelectric coefficient of $d_{33} = 555$ pC $N^{-1}$ [19]. Perovskite materials come in various categories, like ferroelectric [16], pyroelectric [17], piezoelectric, and dielectric. Moreover, some of the perovskite materials also exhibit superconductivity [18]. Thus, perovskite materials based on lead have garnered a lot of interest due to their remarkable optoelectronic and piezoelectric characteristics. However, because lead is toxic, its presence raises issues regarding the environment and human health. Consequently, an extensive amount of research has been conducted to harness lead-free perovskite alternatives. Though it is technically possible to produce lead-free perovskites, at this time, their stability and performance are not up to par with lead-based perovskites. Tin (Sn)-based perovskites are one of the most promising lead-free alternatives, despite having drawbacks like decreased efficiency and instability in ambient conditions [20]. Alternative lead-free substitutes include replacing lead ions with alternative elements, including but not limited to bismuth (Bi), manganese (Mn), copper (Cu), strontium (Sr), and iron (Fe) [21]. Thus, efforts are being made to develop lead-free perovskites in order to minimize the risks that lead-based perovskites pose to human health and the environment. Relaxor ferroelectric perovskite materials have been the subject of recent research, especially lead-based relaxor ferroelectric oxides such as the $(_{1-x})Pb(Mg_{1/3}Nb_{2/3})O_3\text{-}xPbTiO_3$ (PMN-PT) solid solution. These substances have distinct piezoelectric and dielectric characteristics [22]. But due to the toxic behavior of lead, lead-free perovskite materials are preferred and have become the major subject of research. Lead-free perovskites, such as tin-based perovskites, have become attractive substitutes for lead-based perovskites due to their lack of toxicity and still having good optoelectronic qualities [20]. An environmentally responsible and sustainable solution for a range of applications, such as energy harvesting technologies, is the objective of the research and development of lead-free replacements [23]. Thus, lead-free relaxor ferroelectric materials, which offer promising properties for a range of technological applications, are being actively investigated as environmentally friendly substitutes for their traditional lead-based counterparts, such as nanostructured $BaTiO_3$–$Fe_2O_3$–$Bi_2O_3$- and $Bi_{1/2}Na_{1/2}TiO_3$-based relaxor ferroelectric materials, which show potential for storage applications and significant electrostrain [24]. Figure 1 demonstrates the remarkable development of lead-free perovskite materials.

In this review article, we provide a comprehensive overview of the various properties and applications. Our focus is on recent advancements, particularly in enhancing the stability and efficiency of perovskite solar cells. The article also explores non-photovoltaic applications, such as LEDs,
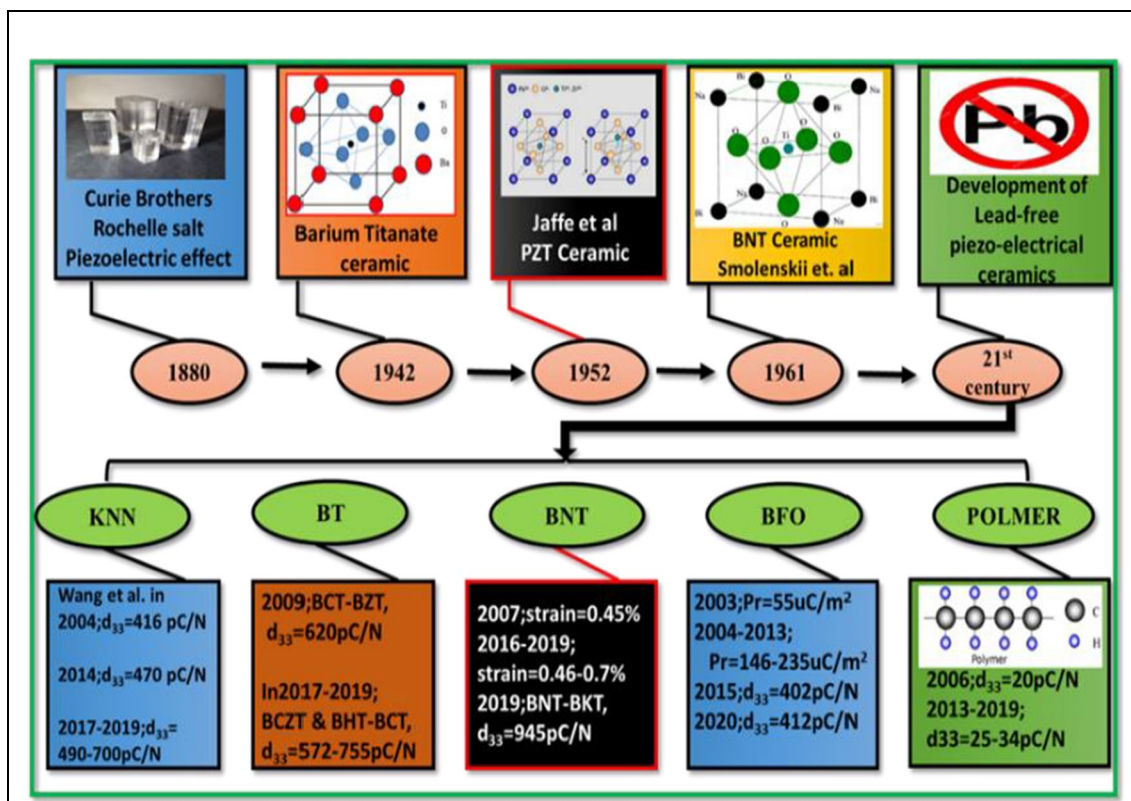
**Fig. 1** Historical evolution and key milestones in the development of piezoelectric materials

thermoelectric devices, and solid oxide fuel cells, showcasing the versatility of perovskite materials. It addresses environmental concerns by discussing lead-free alternatives. Additionally, the review delves into the crystal structure and symmetry of perovskites and highlights their economic feasibility, making it a valuable and up-to-date resource in the field.

## Structure

Perovskites are generally defined as substances with a crystal structure that has the formula $ABX_3$, the same crystal structure as calcium titanium oxide. Gustav Rose made the initial discovery of the mineral in the Ural Mountains of Russia in 1889, and it was given to the Russian mineralogist L.A. Perovski's name. In perovskites, with the general formula $ABX_3$, *A* and *B* are positively charged ions (i.e., cations) and *X* is a negatively charged ion (i.e., anion), where the cations *A* and *B* can span the periodic table and the anion *X* is typically a chalcogen or halogen. Specifically, atoms "A" are larger than atoms "B." The cation with the symbol "A" is divalent, whereas the cation with the symbol "B" is tetravalent. "A" cation is located at the 8 corners, and "B" cations are located at the center of the unit cell. The cation B coordinates with six X anions to generate octahedral geometry,

establishing the cation A in the cubo octahedral location [25]. The oxygen anions are located in six phases of the unit cell. The tetravalent "B" cations are situated within oxygen octahedral structures and occupy the body center position at coordinates (½, ½, ½). The oxygen atoms are located near the face center of the cubic lattice, namely, at the position coordinates (½, ½, 0). The cation exhibits a coordination number of 12 when interacting with anions of X, specifically oxygen. The B cation exhibits a coordination number of 6 with X anions (oxygen). The "X" component can be composed of oxides or other larger ions, including halides, sulfides, and nitrides. The perovskite lattice structure can be compared to a big, positively charged type B cation in the center of a cube. Figure 2 shows the ideal perovskite structure. When the A and B sites are configured as $A_{1(x-1)}A_{2x}$ and $B_{1(y-1)}B_{2y}$, respectively, the X may deviate from the ideal coordination configuration. When the ions in the A and B sites go through changes in their oxidation states, additional perovskite forms may occur. The tolerance factor (*t*) is correlated with the stability of a perovskite-type phase for a given set of cations and anions. This parameter has a big impact on the system's dielectric characteristics and defines its symmetry. Regarding the cation's size limits, tolerance is a variable factor that enables the formation of a phase resembling perovskites. It is given by the expression
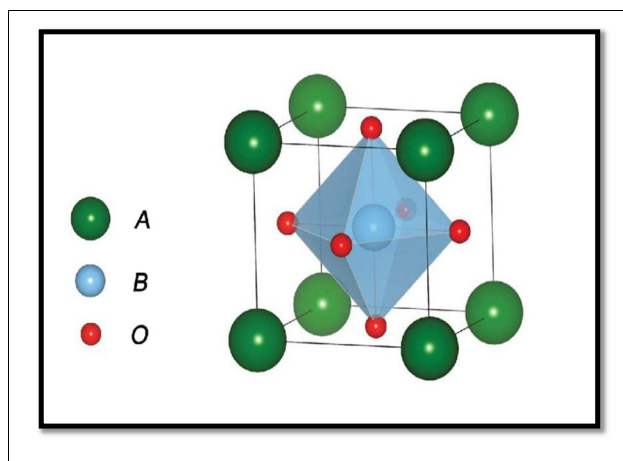
**Fig. 2** Perovskite compounds with a perfect $ABO_3$ structure. Adapted with permission from reference [38]

$$t = (RA + RX)/\sqrt{2}(RB + RX)$$

where $t$ is the tolerance factor, $R_A$ and $R_B$ are the radius of cations A and B ($R_A > R_B$), and $R_X$ is the radius of the anion. When the $t$ value is close to 1, the ideal cubic structure with a perovskite phase is formed, although some perovskite structures can form in the range of 0.90 and 1.10, as in the case of $BaZrO_3$ ($t = 1.01$, cubic) and $CaTiO_3$ ($t = 0.97$, pseudo-orthorhombic monoclinic) [26–29]. Different crystallographic configurations are produced when cations or anions are partially or completely replaced in perovskites, causing disruption of the cubic structure. The properties of perovskite materials are determined by the arrangement of numerous elements in their atoms. Changes in specific atomic arrangements cause a number of phase transitions,

which have a wide range of electronic, optical, and chemical properties with significant characteristics like ferroelectricity, piezoelectricity, nonlinear optical behavior, and so forth [30–34]. Because of their adaptable chemistry and properties, perovskites have emerged as excellent materials in solid-state physics. Researchers are interested in perovskites because of their potential applications in electronics, optoelectronics, medicine, optics, and detectors, among other fields [35–37].

## Crystal symmetry

There are thousands of crystals in nature, but they can be grouped into only 230 space groups based on symmetry elements. If we only look at the orientations of symmetry elements, we can narrow down the macroscopic symmetry elements in crystals to a few key types: a center of symmetry, a mirror plane, rotation axes with onefold, twofold, threefold, fourfold, and sixfold symmetry, and inversion axes with onefold, twofold, threefold, fourfold, or sixfold symmetry. The combination of these distinct symmetry elements results in the macroscopic symmetry of points or point groups [39]. These point groups, a total of 32 in number, are further categorized into seven fundamental crystal systems. In order to increase symmetry, these systems are triclinic, monoclinic, orthorhombic, tetragonal, rhombohedral (also called trigonal), hexagonal, and cubic. Figure 3 shows all possible combinations in the case of the 32-point groups.

Crystallography researchers use different kinds of symmetry elements to describe how orderly points in space are. For example, think about the center of a unit cell, which consists of four symmetry elements, viz., (1) a center of symmetry, (2) axes of rotation, (3) mirror planes, and (4) combinations of these. Using symmetry elements, all crystals can be divided into 32 distinct classes or point groups, of which 21 are non-centrosymmetric, which is an essential requirement

**Fig. 3** Interrelationship of piezoelectric and subgroups based on symmetry
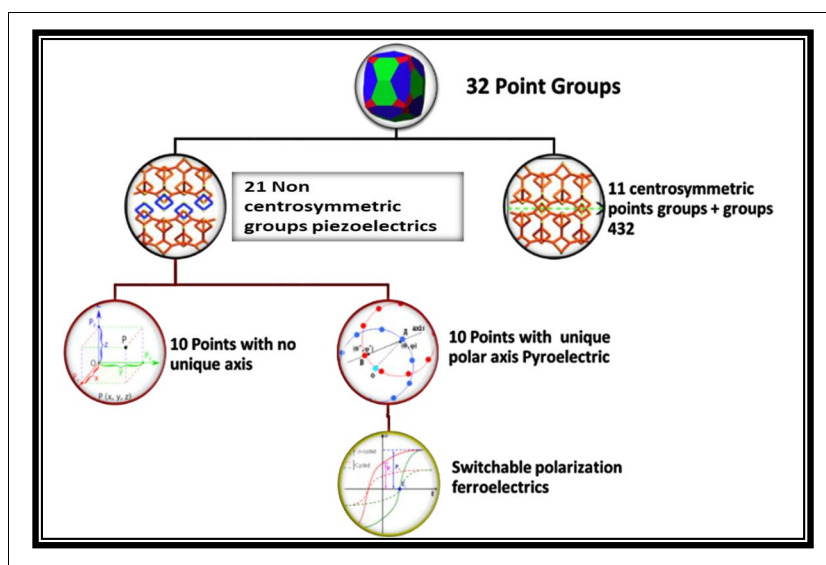
for piezoelectricity to exist in any material. Twenty non-centrosymmetric materials showed bulk piezoelectric effects [40]. One important factor in establishing the existence of piezoelectricity is the lack of a symmetry center. This is because, under homogeneous stress, the symmetry remains central, preventing the emergence of an asymmetrical outcome, such as a vector-like polarization. In essence, a material cannot exhibit polarization arising from the net movement of positive and negative ions in response to stress unless it lacks a center of symmetry. In such cases, stress induces the displacement of ions, giving rise to electric dipoles and subsequent polarizations. When there is an application of stress, the polarization is developed spontaneously and is maintained as permanent dipoles in the structure. This type of reaction is known as piezoelectricity, and it occurs because the polarization shifts as temperature changes. The impact of piezoelectricity is linear

and reversible, and the amount of polarization is dependent on the magnitude of the stress. Additionally, the sign of the charge that is created is based on the kind of stress that is applied, which can be tensile or compressive. Figure 4 shows the relative amplitude and direction of the axial ZFS vectors in each phase of $ABO_3$ for three local symmetry cases: defect dipole, paraelectric ion centered in the oxygen octahedron, and paraelectric center shifted along polarizability.

## Symmetry in perovskites

Perovskite structure is generally taken as simple cubic, which can be lowered to orthorhombic or tetragonal in many cases [42]. The 32-point group symmetry for the perovskite materials is discussed in Table 1. The structure of perovskite crystals can be identified by the generic chemical formula $ABX_3$. When
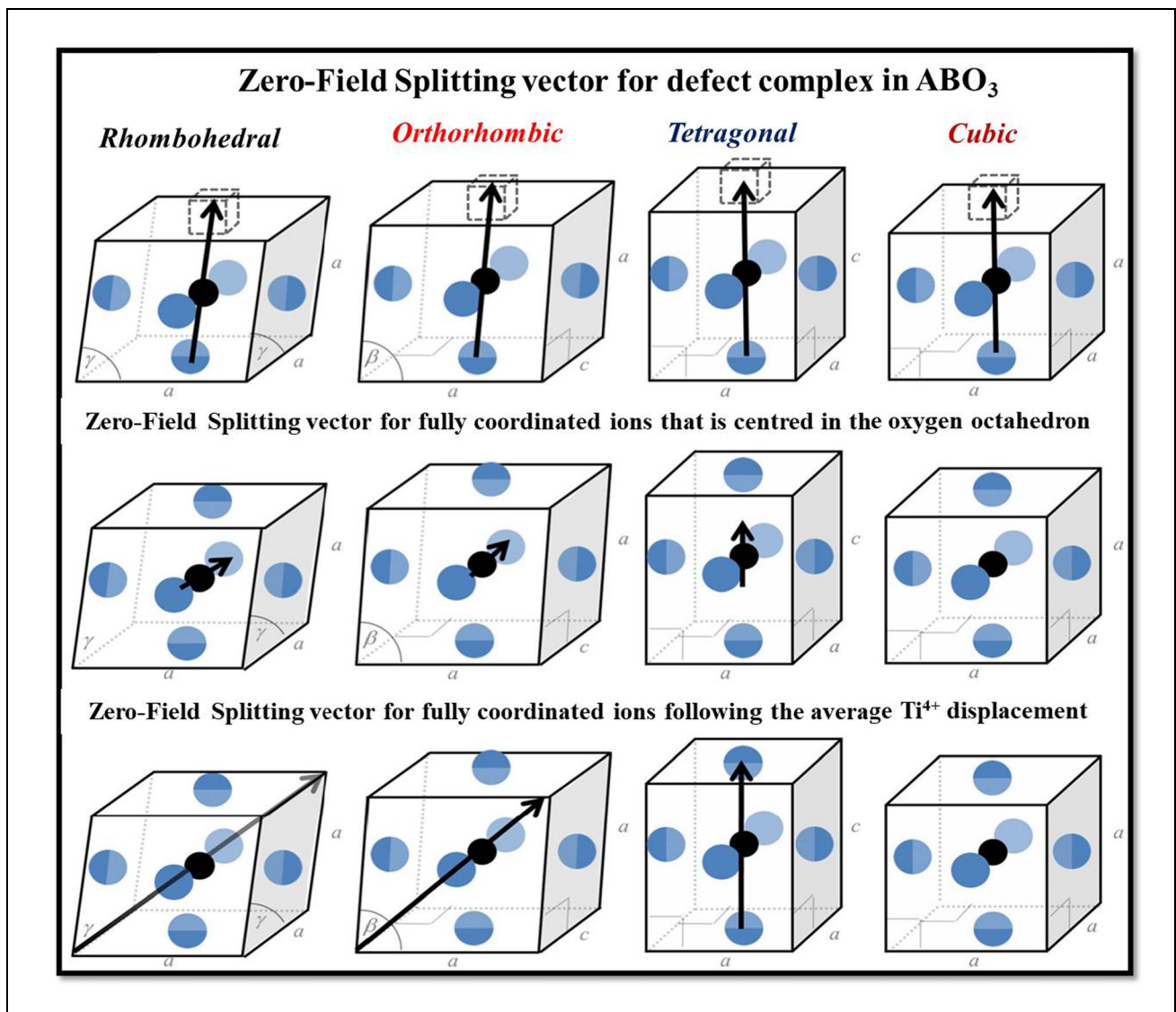


**Fig. 4** The relative amplitude and direction of the axial ZFS vectors in each phase of $ABO_3$. Adapted with permission from reference [41]

looking at $A^{3+}B^{3+}O_3$ perovskites, the rhombohedral R3c shape emerges as the most symmetrical of the available options. This structure is displayed by minerals such as $LaAlO_3$, for example. To construct this structure, the $BO_6$ octahedra must rotate with respect to the cubic framework. It should be noted that this deviation from perfect cubic symmetry is negligible [100].
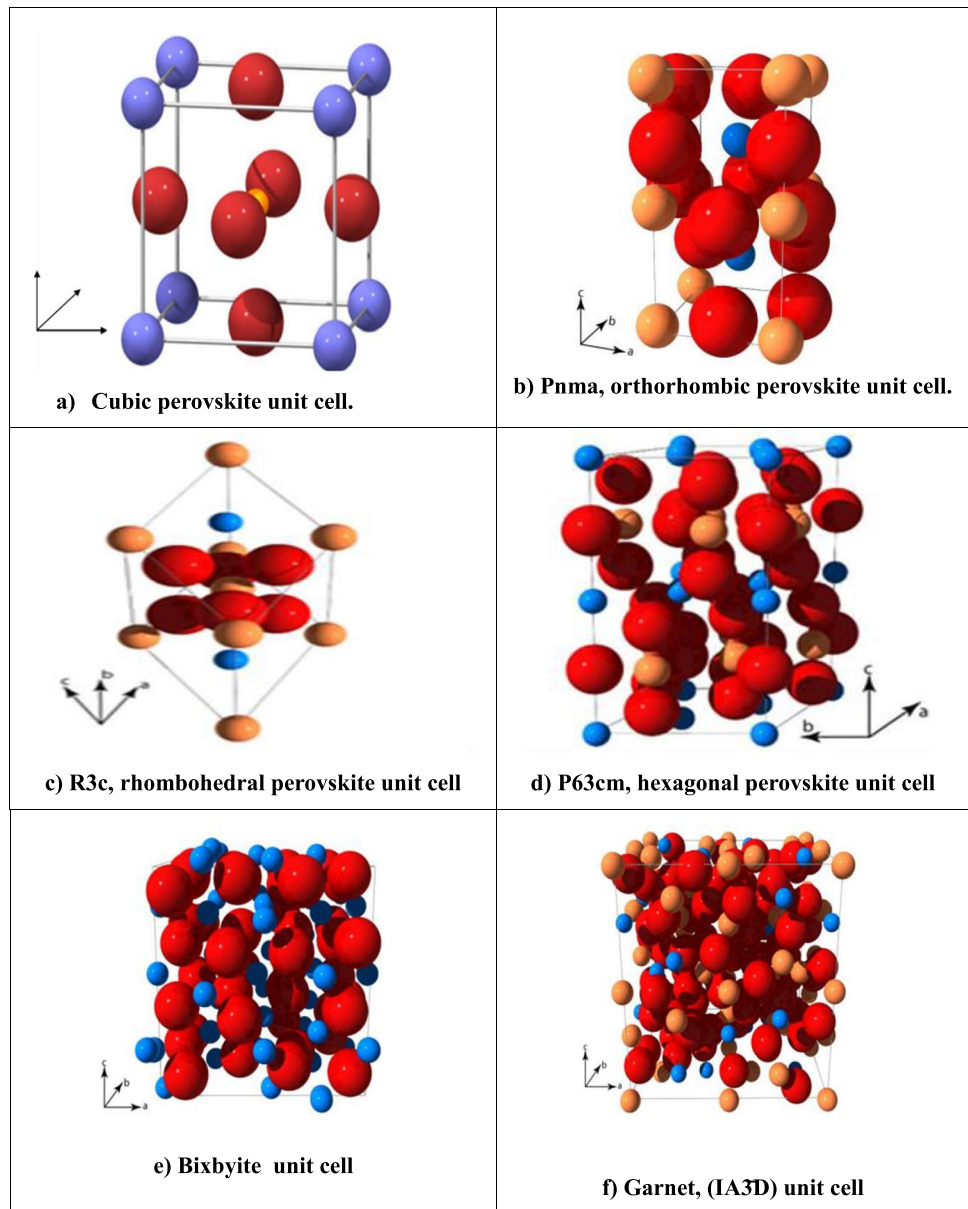
The structure of an ideal cubic perovskite is shown in Fig. 5a. The space group linked with the cubic lattice of perovskite is denoted as Pm-3 m (221). However, at ambient temperature, most of the materials acquire a distorted orthorhombic crystal structure with the space lattice groups Pnma and Pbnm. In the orthorhombic structure, the octahedra tilt is along the $b$ and $c$ axes, whereas this tilt is along all the axes in the rhombohedral structure. This octahedron tilting is influenced by the sizes of the A and B cations, with $AGaO_3$ exhibiting

more distortion than $AAlO_3$. As shown in Fig. 5e, a cubic bixbyite structure with the space group (Ia3) forms, and this is beyond a certain hexagonal region. In this structure, the cation sites are octahedrally coordinated with oxygen, and the difference between the A and B lattice sites is negligible. The unit cell of garnet, $A_3B_5O_{12}$, is shown in Fig. 5f. This structure can be conceptualized as a distorted cubic, close-packed arrangement of oxygen atoms characterized by isometric symmetry [44]. In this configuration, the alternating of shared corners between $BO_6$ octahedra and $BO_4$ tetrahedra collectively forms a framework for the overall structure. It is interesting to notice that, despite the striking changes in crystallographic phases that were expected (from rhombohedral to orthorhombic to hexagonal to bixbyite), the contours of lattice energy remain continuous across these phase boundaries. As a result of this,

**Table 1** The 32-point group symmetry for the perovskite materials is discussed in Ref. [43]

| System | Class | | Symmetry elements |
|---|---|---|---|
| | International | Schönflie ß | |
| Triclinic | 1 | $C_1$ | E |
| | $\bar{1}$ | $C_i$ | $E_i$ |
| Monoclinic | m | $C_s$ | $E\,\sigma_h$ |
| | 2 | $C_2$ | $E\,C_2$ |
| | 2/m | $C_{2h}$ | $E\,C_{2}\,i\sigma_h$ |
| Orthorhombic | 2mm | $C_{2v}$ | $E\,C_{2}\,\sigma'_{v}\sigma''_{v}$ |
| | 222 | $D_2$ | $E\,C_2\,C'_2\,C''_2$ |
| | mmm | $D_{2h}$ | $E\,C_2\,C'_2\,C''_2\,i\sigma_h\sigma'_v\sigma''_v$ |
| Tetragonal | 4 | $C_4$ | $E\,2C_4\,C_2$ |
| | $\bar{4}$ | $S_4$ | $E\,2S_4\,C_2$ |
| | 4/m | $C_{4h}$ | $E\,2C_4\,C_2i\,2S_4\sigma_h$ |
| | 4mm | $C_{4v}$ | $E\,2C_4\,C_2\,2\sigma'_v\,2\sigma_d$ |
| | $\bar{4}$ 2m | $D_{2d}$ | $E\,C_2\,C'_2\,C''_2\,2\sigma_d\,2S_4$ |
| | 422 | $D_4$ | $E\,2C_4\,C_2\,2C'_2\,2C''_2$ |
| | 4/mmm | $D_{4h}$ | $E\,2C_4\,C_2\,2C'_2\,2C''_2\,i2S_4\sigma_h\,2\sigma'_v\,2\sigma_h$ |
| Trigonal (rhombohedral) | 3 | $C_4$ | $E\,2C_3$ |
| | $\bar{3}$ | $S_6$ | $E\,2C_3i\,2S_6$ |
| | 3m | $C_{3v}$ | $E\,2C_3\,3\sigma_V$ |
| | 32 | $D_3$ | $E\,2C_3\,3C_2$ |
| | $\bar{3}$ m | $D_{3d}$ | $E\,2C_3\,3c_2\,I\,2S_6\,3\sigma_d$ |
| Hexagonal | $\bar{3}$ m | $C_{3h}$ | $E\,2C_3\,\sigma_h\,2S_3$ |
| | 6 | $C_6$ | $E\,2C_6\,2C_3\,C_2$ |
| | 6/m | $C_{6h}$ | $E\,2C_6\,2C_3\,C_2\,i\,2S_3\,2S_6\,\sigma_h$ |
| | $\bar{6}$ m2 | $D_{3h}$ | $E\,2C_3\,3C_2\,\sigma_h\,2S_3\,3\sigma_v$ |
| | 6mm | $D_{6v}$ | $E\,2C_6\,2C_3\,C_2\,3\sigma_v\,3\sigma_d$ |
| | 622 | $D_6$ | $E\,2C_6\,2C_3\,C_2\,3C'_2\,3C''_2$ |
| | 6/mmm | $D_{6h}$ | $E\,2C_6\,2C_3\,C_2\,3C'_2\,3C''_2\,2S_3\,2S_6\,\sigma_h\,3\sigma_d\,3\sigma_v$ |
| Cubic | 23 | T | $E\,4C_3\,4C^2_3\,3C_2$ |
| | m3 | $T_h$ | $E\,4C_3\,4C^2_3\,3C_2\,i\,8S_6\,3\,\sigma_h$ |
| | $\bar{4}$ 3m | $T_d$ | $E\,8C_3\,3C_2\,6\sigma_d\,6S_4$ |
| | 432 | O | $E\,8C_3\,3C_2\,6C'_2\,6C_4$ |
| | m3m | $O_h$ | $E\,8C_3\,3C_2\,6C'_2\,6C_4i\,8S_6\,3\,\sigma_h\,6\,\sigma_d\,6S_4$ |

**Fig. 5** Pictorial representation of various perovskite unit cells



a) Cubic perovskite unit cell.

b) Pnma, orthorhombic perovskite unit cell.

c) R3c, rhombohedral perovskite unit cell

d) P63cm, hexagonal perovskite unit cell

e) Bixbyite unit cell

f) Garnet, (IA3D) unit cell

the lattice or internal energy experiences relatively slight alterations in conjunction with the modifications in the crystalline structure. This phenomenon is illustrated by the decrease in the tolerance factor from the dominance of the rhombohedral structure, which is observed when the A cation radius is relatively high and the B cation radius is low, to the point where the bixbyite structure is energetically preferred [45].

## Classification of perovskites

Perovskite structures are possible in numerous forms, such as oxides, sulfides, and nitrides, depending on their ability to occupy different anionic and cationic sites. Perovskites exhibit four dimensionalities, i.e., zero, one, two, and three dimensionalities that exist in different forms, e.g., (a) $ABX_3$ perovskites (e.g., $CaTiO_3$ and $CH_3NH_3PbI_3$), (b) $A_2BX_4$ layered perovskites (e.g., $Cs_2PbI_4$ and $K_2NiF_4$), (c) $A_2BB'X_6$ double perovskite (e.g., $Ba_2TiRuO_6$), and (d) $A_2A'B_2B'X_9$ triple perovskites (e.g., $Ba_2KNaTe_2O_9$) [46, 47]. Several cation/anion combinations can be used to create distinct forms by preserving charge neutrality, for example, $A^+B^{5+}$, $A^{2+}B^{4+}$, and $A^{3+}B^{3+}$. A vast array of oxides, halides, sulfides, and nitride compounds can be created by arranging more than 90% of the elements of the periodic table in the aforementioned forms. Numerous of these compounds have remarkable qualities that make them valuable for energy-related devices. Perovskites are basically of two types: perovskite-type oxides and metal halide perovskites. Owing to their favorable chemical and physical characteristics,

perovskite-type oxides (PTO) exhibit exceptional features such as catalytic activity for the oxygen evolution reaction (OER) and oxygen reduction reaction (ORR) [48, 49]; electronic conductivity [50, 51]; oxygen ion mobility across the crystal lattice [52]; super magnetic properties; and dielectric, metallic, and semiconducting behaviors [53, 54]. PTO is widely used in energy storage applications because of its high conductivity towards lithium ions (Li-ion). Similar to PTO, crystals of metal halide perovskite (MHP) are formed with the general formula $ABX_3$ ($X = ¼$ halogen), where halogen anions, metal cations, and organic cations are represented by $A$, $B$, and $X$, respectively. The following subsections give a brief overview of the physical, chemical, and structural characteristics of perovskite-type oxides (PTO) and metal halide perovskite (MHP) [55].

## Perovskite-type oxide

Perovskite can be found in many different forms, including the oxides and sulfides described in the previous heading. Perovskite oxides (PO) have good catalytic performance for the $O_2$ evolution reaction (OER) and $O_2$ reduction reaction (ORR), electrical properties due to their excellent characteristics [50, 56], super magnetic characteristics [57], as well as $O_2$ ion mobility across the crystal structure [52], insulating, metallic, and semiconducting behaviors. A variety of oxides of transition metals with the simple formula $ABO_3$ is included in the perovskite oxide (PO) group. Typically, a cubic structure can be found in these oxides. Hexahedral, tetrahedral, orthorhombic, and rhombohedral forms are all possible transformations that are due to variations in physical environments such as temperature and pressure and also due to structural variations in perovskite oxides, and different magnetic ordering can be realized [58]. The metallic, catalytic, piezoelectric, ferroelectric, superconductivity, and magnetic properties can be changed with the appropriate doping PO or by substituting anion/cation. Due to their wide range of capabilities, PTOs are utilized in many different types of electronic devices, including biosensors, transducers, actuators, LED screens, random access memory, solar cells, wireless technology, frequency-controllable microwave instruments, piezoelectric devices, and supercapacitors [59]. Perovskite oxide (PO) appears to be widely recognized for its application as catalysts in hydrogen lysis, oxidation/reduction, and hydrogenation processes. In recent years, the PO has seen an increase in its use in the fields of geosciences, material physics, energy, and catalysis [60]. PO are employed in solar cells and supercapacitors because of their appealing properties, which include lattice defects, lattice planes that are exposed, consistent surface features, NP scales, and a comparatively large surface with mesoporosity [61].

## Metal halide perovskites

Metal halide perovskites (MHPs) have been recognized as low-cost, high-efficiency optoelectronic semiconductors for next-generation devices because of these advantageous qualities. The use of MHPs has brought about the development of PSCs, or perovskite solar cells. The most advanced PSCs now have a power conversion efficiency (PCE) comparable to the finest crystalline silicon solar cells. $CH_3NH_3PbX_3$ and $CsPbX_3$ ($X = Cl$, Br, or I) are a couple of the significant MHPs. MHPs have a tolerance factor that is close to 1, just like PTOs, indicating that they have the ability to sustain a symmetrical and stable structure. Many reports have stated that MHPs can be obtained under specific temperature conditions in three different phases: orthorhombic: $T \leq 165$ K; tetragonal: $165 < T \leq 327$ K; cubic: $T > 327$ K. Additionally, MHPs can introduce a superlattice to automatically create buffer layers at boundaries and self-adjust the phase configuration [62, 63]. MHPs exhibit exciting emissions, high absorption coefficients, and a tunable energy band gap. MHPs are therefore categorized as common semiconductor materials with a direct band gap. Additionally, MHPs exhibit tunable and transparent photoluminescence at room temperature, which is achieved through modifications to organic molecules or halide anions. MHPs are materials with a broad range of applications for light-emitting devices, such as lasers, LEDs, and optical sensors, because of their tunable bands, such as emission and absorption [64]. Polycrystalline thin films composed of MHPs, for instance, are easier to produce and have fewer defects than standard semiconductor films. MHP thin-film synthesis has drawn a lot of attention due to its significance in a number of optoelectronic applications [65]. A vast array of devices have made use of nanomaterials derived from MHP [55]. Perovskite materials can be made via a variety of methods, such as the sol–gel process, spray and freeze drying, carbonization, hydrothermal, and solid-state reactions.

## Synthesis methods

The growing interest in nanoparticles as a result of their distinctive size- and shape-dependent optical, electronic, and biochemical properties emphasizes the need for easy-to-use and novel techniques to control the morphologies of nanoparticles in an efficient manner [66, 67]. Materials that are either organic or inorganic and have at least one dimension between 1 and 100 nm in diameter are referred to as nanoparticles [66]. In general, there are two main approaches for synthesizing nanoparticles: the bottom-up approach and

the top-down approach. Figure 6 depicts the diagrammatical illustration of bottom-up and top-down approaches.

- Bottom-up approach. One of the most popular techniques for synthesizing large amounts of particles with a variety of sizes and shapes is this one. Using this process, atoms, ions, and organic molecules come together to form bigger structures. This method yields homogenous, uniformly shaped nanoparticles with a narrow size distribution and fewer surface flaws. Therefore, in order to prepare well-defined nanoparticles for biotechnological applications, a bottom-up approach is typically employed. Solution phase synthesis, vapor phase synthesis, and self-assembled organic materials in the form of micelles, vesicles, polymersomes, and cross-linked nanoparticles are a few examples of bottom-up approaches for nanoparticle synthesis [67].

- Top-down approach. It uses attrition and milling to mechanically break down big materials into smaller nanoparticles. The impure nanoparticles produced by the top-down method have surface crystallographic damage and defects in their materials. In addition, a wide range of particle shapes and sizes are present in the generated heterogeneous nanoparticles. These particles are mostly used in the preparation of nanograined bulk material coatings to increase the wear and tear resistance of automotive and surgical implants due to poor control over particle size and large surface defects [68]. In the last few years, "bottom-up" production methods have become more and more popular. Bottom-up methodology pertains to the process of building material from the bottom up, either cluster by cluster, molecule by molecule, or atom by atom. Both strategies are crucial to contemporary industry, and
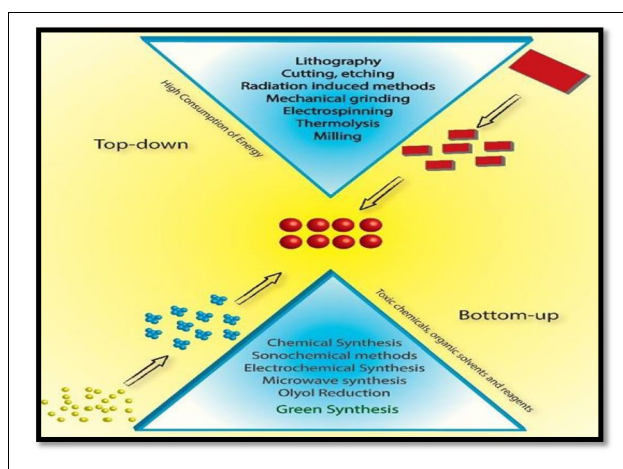


**Fig. 6** Schematic representation of top-down and bottom-up approaches for nanoparticle synthesis. Copyright and permission [69]

they also have a place in nanotechnology. The two primary approaches can further be divided into a number of methods for the preparation of nanomaterials.

## Solid state reaction method

Ceramic materials are made utilizing a range of old and novel methods, including hydrothermal synthesis, spray drying synthesis, wet chemical route, sol–gel method, and solid-state reaction method. The solid-state reaction technique is commonly used to generate polycrystalline materials because it is simple, inexpensive, and successful. This is a direct reaction approach in which high temperatures are used to provide the needed temperature between precursors, which are normally in powder form. Solid-state reactions are typically slow because, unlike gas-phase reactions, they involve a lot of bond breaking and ion migration through the solid. According to the approach, the reaction does not start until the temperature hits at least 2/3 of one of the reactants' melting points. In the solid-state reaction procedure, the initial reagents used are oxides and carbonates with high purity, which are weighed in accordance with the desired compound's stoichiometry while taking moisture and impurity amounts into account. Raw material impurities have an impact on the dielectric, conductive, and piezoelectric properties in addition to reactivity [70]. To control particle size and produce a homogeneous mixture, raw ingredients are mechanically combined, followed by a grinding operation. As a wetting medium, ethanol is used because it is inexpensive and available with enough purity. All the raw materials were weighed according to their stoichiometric proportion and milled in ethanol medium continuously using an agate mortar and pestle. This liquid is used for a homogeneous mixture of precursors to escape the formation of the secondary phase. Mixing is generally done by a ball mill, and the method may take several hours. After grinding and mixing the starting materials for the required time, the calcination of the mixture is being done. Calcination is a heat treatment process in the existence of oxygen applied to solid resources to bring about a thermal decomposition, phase transition, or elimination of a volatile segment. It normally takes place at high temperatures, but below the melting point of the product materials. In general, four physical processes are involved in the calcination of the raw materials: linear expansion of the particles ($<400$ °C), solid phase reaction (400–750 °C), contraction of the product (750–850 °C), and grain growth ($>850$ °C). The calcined powder is again grinded and crushed to reduce its size, which also enhances densification during the sintering process [71]. Ceramic processing has profound effects on the microstructure and electrical properties of the given material. The effects are the purity, crystal forms, and particle size of the raw materials; the reactivity of the mixed materials, the grinding method; and control against impurity pick-up and particle size.

## Sol–gel method

Initially, for the preparation of glass and ceramic materials at low-temperature sol-gel method was developed. In the sol-gel method, firstly, the hydrolysis of the metal alkoxide solution with water or alcohol takes place in the presence of an acid or base, which is then followed by polycondensation. With the removal of the water molecules in the solution, the liquid phase gets changed into the gel phase, and there is also an increase in the viscosity of the solution due to polycondensation. The gel phase changes into the powder phase after all the water molecules are condensed. To get the fine crystalline nature of the powder, some additional heat is required. The sol-gel method is very useful to prepare oxides, composites, and hybrids of organic and inorganic materials. Inorganic polymerization reactions are the basis of the sol-gel method. Its simple procedure is the main advantage of this method [72].

## Co-precipitation

This is a straightforward, widely used method for creating a wide range of nanoparticles. The precipitation process in this method requires an aqueous medium. This procedure can be used to produce uniform nanoparticles. To summarize, the co-precipitation technique involves combining two or more salts of water-soluble metal ions, usually divalent and trivalent ones. The soluble salts are primarily found in the trivalent metal ions found in them. These soluble salts react and are reduced, resulting in the precipitation of at least one insoluble salt. It is necessary to constantly stir the solution, which may or may not adhere to the heat conditions depending on the reducing agent and reaction conditions. The degree of crystallinity in the particles can be increased by applying heat energy. By adding common reducing agents like sodium hydroxide, ammonia solution, and many more to keep the pH at the required level, the entire process is kept in an alkaline medium. The ratio of salt used, the pH of the solution, the temperature of the reaction medium, and the type of base used—all of which can be controlled by filtration or centrifugation—all affect the size of the nanoparticles. The solvent can then be extracted, dried, and further purified. Nucleation, growth, coarsening (Ostwald ripening), agglomeration, and stabilizing processes are the steps in this method that lead to the formation of nanoparticles. They primarily involve the processes of nucleation and growth. A new thermodynamic phase's smallest elementary particles appear through a process known as nucleation. The degree of supersaturation is a key factor in the nucleation process. The solution has more dissolved materials in it than the solvent could dissolve when it is in a supersaturation state. The solute thus has a solubility that is greater than equilibrium. In the process of growth, larger particles will eat smaller

ones in order to lower their surface energy. Particle growth beyond the nanoscale may occur if coarsening and agglomeration are not controlled. Certain stabilizing or capping agents are useful in stopping the growth of nanomaterials. Through the chemisorption of charged species, the capping agents attach to the nanoparticle surface and cause an electrostatic (van der Waals) repulsion to form on its surface. Stable nanoparticles will form if the repulsive forces are strong, or else coagulation will take place [72].

## Microwave assisted

The microwave-assisted technique was developed in the 1950s, but it has only gained widespread recognition in the past 20 years. By employing EMR to heat the materials with moveable electric charges, microwave radiations are directly transferred to the materials. Thermal energy is produced in this process from electromagnetic energy. As a result of the use of frequencies between 1 and 2.5 GHz, temperatures between 100 and 200 °C will rise. It necessitates a quicker reaction time in order to finish more laborious reactions in a matter of minutes. It is possible to prepare small-size particles with a narrow size distribution using this method. This technique is used to prepare ferrites, oxides, selenides, and colloidal metals [72].

## Hydrothermal technique

The reaction occurring in solvents contained in sealed vessels by heating them to their critical point under autogenous pressure is called the hydrothermal/solvothermal process. In this method, the solutions are subjected to high pressure and temperature. The main advantage of this method is the preparation of good-quality crystals while controlling their composition. In 1:2 mol ratios, the divalent and trivalent transition metal salts are mixed together [73–75]. To get a homogeneous solution, mix the organic solvent with constant stirring in the above solution. Stirring this solution at room temperature yields a low-viscous gel. Then, the solutions are brought into the sealed vessel, commonly called an autoclave (bomb). By heating, an autogenous increase in pressure takes place, which will directly raise the solvents above their boiling points. The temperature adjustment and time are dependent on the type of nanoparticles to be synthesized. After the hydrothermal treatment by varying the time and temperature, the sample thus prepared is filtered and washed, followed by drying, which gives us the desired crystalline powder. This is a good method for the preparation of the least-size nanoparticles, which can be applied in the biological field. Through the selection of suitable solvents and also by varying factors like temperature, pressure, pH, aging time, the concentration of reactants, and the time of the reaction, the controlled and desired size, morphology,

and surface chemistry of nanoparticles will be produced. Highly homogeneous nanoparticles can be achieved by using this technique. Without post-annealing treatments, the development of the least-size nanoparticles in the desired crystalline phase at relatively lower temperatures is possible with this method. This attracted so many researchers than the traditional methods. By using this method, single crystals, zeolite oxides [76], and single crystals, many doped metals, selenides, and sulfides are prepared [72]. Figure 7 demonstrates the various synthesis methods being used for the preparation of perovskite nanomaterials.

# Properties

## Phase transition

The various phases and structural transitions exist when there is a change in temperature. Specifically, these transitions include a cubic phase occurring above 120 °C, followed by a tetragonal phase between 120 and 5 °C, an orthorhombic phase between 5 and −90 °C, and ultimately a rhombohedral phase below −90 °C. Notably, during the rhombohedral phase, the crystal's polar axis is aligned with a body diagonal [77]. Below the Curie temperature, which defines the transition from ferroelectric (FE) to paraelectric (PE) phase, the crystal structure deforms into the tetragonal
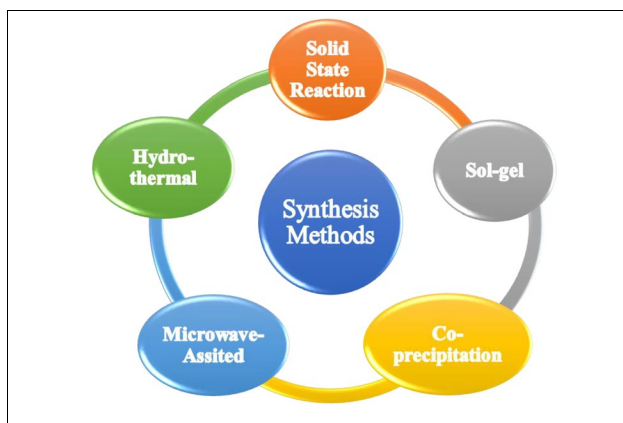


**Fig. 7** A visual depiction of various innovative techniques for synthesizing perovskite materials

phase, resulting in spontaneous polarization and ferroelectric and piezoelectric behavior. $BaTiO_3$ exhibits distinct phases depending on temperature variations. It acquires a paraelectric cubic phase above its Curie point, approximately at 120 °C. In the temperature range from 130 to 0 °C, it stabilizes into a ferroelectric tetragonal phase with a c/a ratio of approximately 1.01. The spontaneous polarization in this phase aligns with one of the [001] directions from the original cubic structure. $BaTiO_3$ assumes a ferroelectric orthorhombic phase transition between 0 and −90 °C, with polarization along one of the [109] directions in its original cubic structure. When the temperature falls below −90 °C, an orthorhombic to ferroelectric rhombohedral phase transition occurs, with polarization following one of the [110] cubic orientations. This spontaneous polarization below the Curie temperature ($T_C$) results from changes in the crystal structure [78, 79]. Table 2 shows the substitution of various dopants and their influence on phase transition. The cubic phase displays paraelectric characteristics and has a very small dielectric constant, but the tetragonal phase indicates ferroelectric characteristics, which are more useful for dielectric applications due to its high dielectric constant [80].

where ↓ is the decrease, ↑ is the increase, and → is the unchanged.

Perovskite materials find utility across a diverse array of applications, including capacitors, non-volatile memories, actuators, sensors, piezoelectric devices, ultrasonic equipment, underwater technologies, high-temperature heating systems, frequency filters for wireless communications, and more. Perovskite materials can be nano-crystalline, bulk, thin films, or rods, depending on their application [84]. Several factors make perovskite-type structures functional, such as non-stoichiometric arrangements of cations and anions, irregular cation configurations, and an electronic structure with mixed valences. These structures support most periodic table metals. Multicomponent perovskites ($ABO_3$) can be synthesized by partially substituting cations in the A and B locations. This technique creates complex, multifaceted materials in a perovskite-type oxide structure. These properties make perovskite materials distinctive. Ferroelectricity allows spontaneous electric polarization that may be reversed with an electric field [85–87]. Figure 8 shows an example of different phase transitions of $BaTiO_3$.

**Table 2** Substitutions and their influence on phase transition

| Material | Substitution | Site | Ionic radii | $T_{R-O}$ | $T_{O-T}$ | $T_c$ | Ref |
|---|---|---|---|---|---|---|---|
| $BaTiO_3$ | $Ca^{2+}$ | | 0.100 | ↓ | ↓ | → | [81–83] |
| | $Sr^{2+}$ | A | 0.118 | ↓ | ↓ | ↓ | |
| $Ba^{2+}$:0.135 | $Zr^{4+}$ | | 0.072 | ↑ | ↑ | ↓ | |
| | $Sn^{4+}$ | B | 0.069 | ↑ | ↑ | ↓ | |
| $Ti^{4+}$:0.06 | $Hf^{4+}$ | | 0.064 | ↑ | ↑ | ↓ | |

## Piezoelectricity

The Nobel laureates Pierre and Jacques Curie first identified the piezoelectric phenomena in 1880 by measuring surface charges that appeared on various crystals under stress, including tourmaline, quartz, and Rochelle salt. A resurgence of intense research and development into piezoelectric devices was inevitably sparked by the discovery of inexpensively produced piezoelectric ceramics with astounding performance characteristics, which led to their wide-ranging applications. One of them, barium titanate ($BaTiO_3$) ceramic, was found to have a gigantic dielectric constant of 1100, which was ten times greater than the greatest value at the time, rutile $TiO_2$. Due to the discovery of several additional piezoelectric ceramics, including led niobate piezoelectric ceramics in 1952 and lead zirconate titanate (PZT) compositions in 1955, the productions that utilized the piezoelectric materials quickly advanced in the late 1950s. Today, a number of piezoelectric ceramics, including $BaTiO_3$, PZT (and modified compositions like (Pb, La) $(Zr,Ti)O_3$, etc.), lead magnesium niobate ($Pb(Mg_{1/3}Nb_{2/3})O_3$, and lead zinc niobate $Pb(Zn_{1/3}Nb_{2/3})O_3$, are widely utilized [88]. Noncentrosymmetric crystals show the phenomenon known as piezoelectricity, in which the application of stress causes the material to acquire an electric polarization. The development of an induced strain, on the other hand, is inversely proportional to an applied electric field. The converse effect is a phenomenon that is used in actuation [89]. Piezoelectricity is a remarkable phenomenon exhibited by certain materials, showcasing their unique capability to produce an electric current in response to the application of mechanical force and, conversely, to convert electrical energy into mechanical motion [90]. This fascinating property results from the interaction between mechanical stress and the electrical charge innate to these materials.

When these substances are subjected to mechanical stress, a remarkable transformation occurs. This transformation results in the separation of positive and negative ions within the material through the creation of electric polarization. These piezoelectric materials can be broadly categorized into two primary groups: crystals and ceramics. The atomic structures of crystals such as quartz and tourmaline are well-ordered, and their piezoelectric properties are pronounced. In contrast, ceramics, such as lead zirconate titanate (PZT), barium zirconate titanate (BZT), and potassium sodium niobate (KNN), exhibit piezoelectric properties due to their unique microstructures and chemical composition. These two distinct classes of piezoelectric materials have numerous applications in a variety of disciplines, including sensors, transducers, actuators, and energy-harvesting devices. The ability to harness mechanical energy and convert it into electrical power has expanded the scope of technological possibilities and contributed to scientific and technological advancements. Some examples are as follows:

- Naturally occurring: quartz, cane sugar, collagen, topaz, Rochelle salt, wood, tendon, etc.
- Man-made crystals: gallium orthophosphate ($GaPO_4$), quartz analogic crystal, lanthanum gallium silicate ($La_3Ga_5SiO_{14}$), quartz analogic crystal, etc.
- Man-made ceramics: barium titanate, lead zirconate titanate etc.

As piezoelectric materials are crystalline and show no characteristics of being piezoelectric in their natural state, a poling condition must exist for the crystalline material to exhibit the piezoelectric effect. Electric diploes align parallel to the direction of the applied field in these materials when they are exposed to a high DC electric field, which polarizes the specimen. Figure 9 shows a detailed diagram

**Fig. 8** Phase diagram of $BaTiO_3$ (copyright permission and copyright clearance center license number: 5030130645203
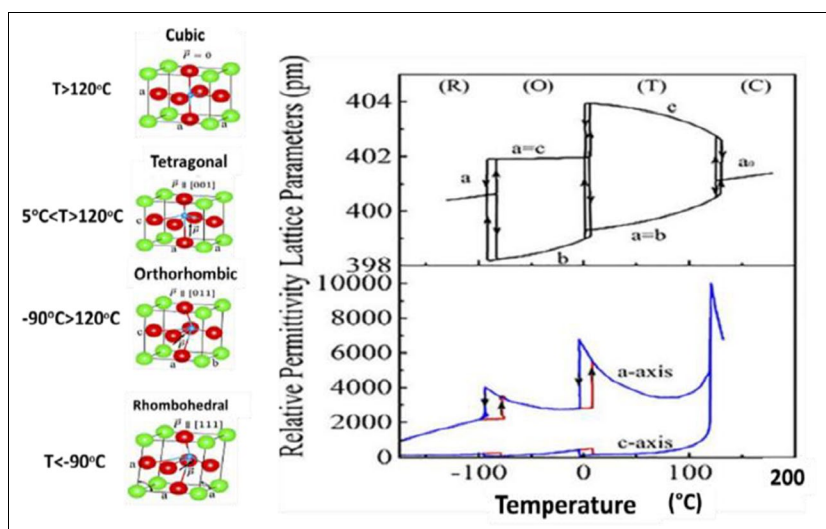
of the material before, during, and after the poling process. Electric dipoles are initially randomly oriented, but during poling, they align themselves in the applied field's direction to produce net polarization. Electric dipoles exhibit a slight deviation from their symmetry after poling, which results in permanent polarization and mechanical deformation, resulting in the specimen's piezoelectricity. Additionally, the substitution or addition of dopants could improve the properties of piezoelectric materials by distorting the crystal structure and its properties [91–93].

PZT is one of the piezoelectric materials that is most widely utilized and exploited for piezoelectric actuators, sensors, transducers, and so on, but it is extremely hazardous and can harm the kidneys, brain, nervous system, and particularly the intelligence of children. Moreover, the volatilization of PbO during the high-temperature sintering process results in instability in the production's composition and electrical properties in addition to environmental degradation. A considerable amount of research has been done to find alternative piezoelectric materials in order to overcome the problem of lead toxicity [88]. As a result, during the past 15 years, research into new lead-free materials has greatly increased. Polarization in a material depends on two primary factors: the magnitude of the applied stress and the nature of the stress, whether it is tensile or compressive. When an external pressure is applied to the material, it produces an electric charge proportional to the magnitude of the applied burden [7, 95]. This means that when a mechanical load is applied, the material will produce an electric charge proportional to the applied load. The pictorial representation of the piezoelectric effect due to tension and compression is shown in Fig. 10. In the compression effect, volume is decreased, and it shows a voltage of the same polarity as the material, whereas in the case of the tension effect, volume is increased, and it shows a voltage opposite to the polarity of the material.

## Pyroelectricity

The pyroelectric phenomenon was first noticed in 400 BC in ancient Greece due to the ability of heated tourmaline crystals to attract small objects [96]. The pyroelectric effect was first studied in relation to its possible origin, particular material performances, and potential applications during the 1930s [97–100]. Since the pyroelectric phenomenon is used in thermal detectors, it has been the subject of extensive research beginning in the 1960s [96, 98, 101]. The term "pyroelectric effect" describes a shift in spontaneous polarization that occurs in some polar materials as a result of temperature fluctuations.



**Fig. 9** Systematic diagram of the poling process. Adapted with permission from reference [94]
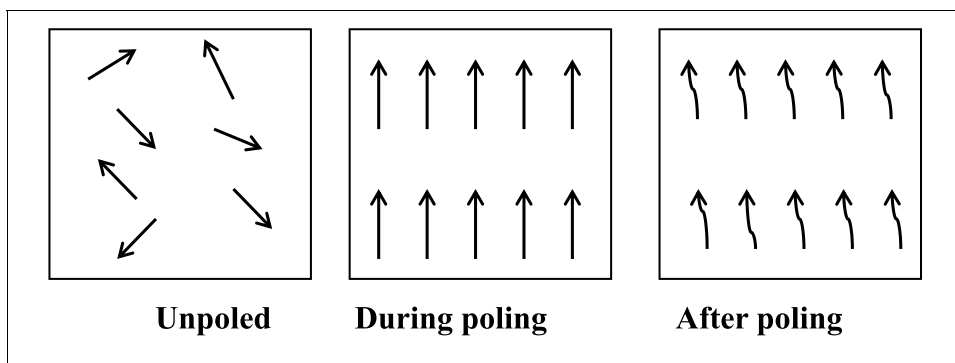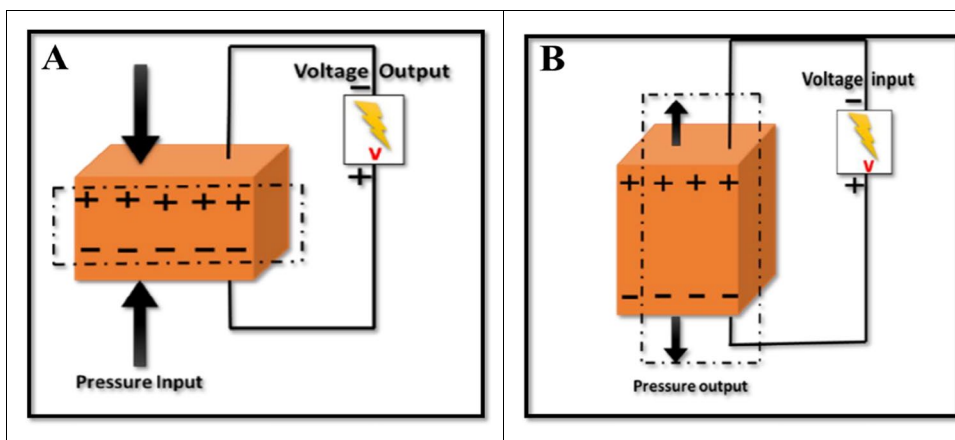


**Fig. 10** The pictorial representation of the piezoelectric effect due to tension and compression

Pyroelectric materials also have their reverse effect, known as an electrocaloric effect, which can alter temperature as a result of polarization variation, much like the piezoelectric and converse piezoelectric effects [102]. One intriguing characteristic of some materials is their capacity to produce an electric potential in response to temperature changes, whether they are heating or cooling. When a material's temperature fluctuates, positive and negative charges within it migrate to opposing ends, causing this fascinating phenomenon. An electrical potential difference and material polarization are the outcomes of this movement [97]. The pyroelectric effect's mechanism is connected to spontaneous polarization. Figure 11 shows the forming principle of the pyroelectric effect. The electric dipoles only vibrate at random in the vicinity of their aligning axes at a constant temperature, which leads to a constant total spontaneous polarization. As the temperature rises, the electric dipoles oscillate at a greater angle, which reduces both the number of bound charges and the overall spontaneous polarization. In order to offset the bound charges, the free charges correspondingly redistribute, creating an electron flow, or pyroelectric current [103, 104]. Paradoxically, a pyroelectric current will also be produced in the opposite direction if the material is cooled instead of heated. Dielectric displacement, or $D$, is defined as follows for dielectrics:

$$D = \frac{Q}{A} = \varepsilon E + P \tag{1}$$

where $Q$ represents the charge, $A$ denotes the electrode sample area, $e$ denotes permittivity, $E$ denotes the external electrical field, and $P$ denotes polarization. The pyroelectric coefficient $p$ can be defined as

$$p = \frac{\partial D}{\partial T} = \frac{\frac{\partial Q}{\partial t}\left(\frac{\partial T}{\partial t}\right)^{-1}}{A} = E\frac{\partial \varepsilon}{\partial T} + \frac{\partial P_s}{\partial T} \tag{2}$$
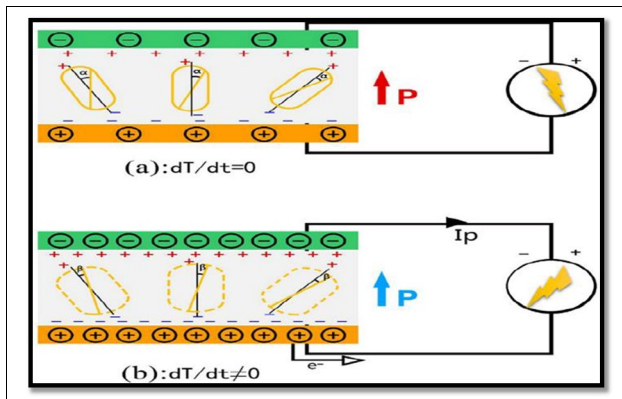
The pyroelectric coefficient, in the absence of an external electric field, can be written as

$$p = \frac{\partial P_s}{\partial T} = \frac{i_p\left(\frac{\partial T}{\partial t}\right)^{-1}}{A} \tag{3}$$

where $i_p$ is the pyroelectric current and $\frac{\partial T}{\partial t}$ is the change in temperature [105]. Pyroelectric current can be measured to determine the pyroelectric coefficient based on Eq. (3), given a sample area and temperature change rate. In pyroelectric applications, pyroelectric ceramics are fairly significant. They have many benefits, such as good mechanical qualities, low cost, easy manufacturing in large areas, and dependable electrical performance. Perovskites with the formula $ABX_3$ are well known for being a very adaptable ceramic host, where the B ions in the center and the A ions at the unit cell's corner are octahedrally and 12-fold coordinated [27, 106, 107]. The middle of each face's X represents oxygen in the majority of common pyroelectric materials [107]. The common understanding of perovskite materials' ferroelectricity is that a permanent electric dipole is created when a B-site ion is displaced from its centrosymmetric position in the unit cell along the $c$-axis [108, 109]. Thus, one can greatly alter the electrical properties by suitably altering the A or B site's composition. In pyroelectric applications, there are numerous significant lead-free ceramic systems, including ceramics based on $BaTiO_3$ and $Bi_{0.5}Na_{0.5}TiO_3$ [97].

Therefore, ferroelectric material (such as $BaTiO_3$) is non-centrosymmetric, piezoelectric, and pyroelectric. In the domain of ferroelectric crystals, these are the crystals that are inherently polar, and the direction of their spontaneous polarization can be altered by the application of an external electric field. Therefore, all ferroelectric materials are pyroelectric by nature. It is essential to observe, however, that not all pyroelectric materials possess this switchable polarization; this is the distinguishing characteristic that separates ferroelectric materials from other pyroelectric materials.
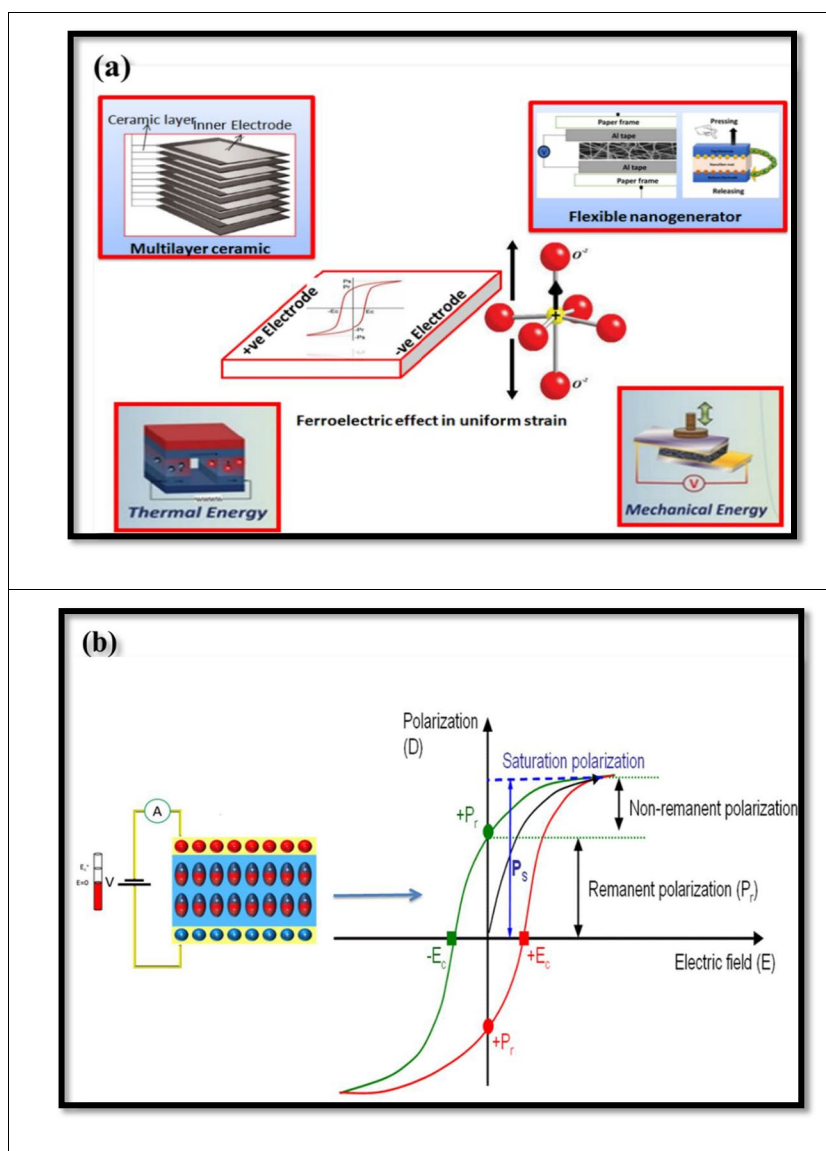
## Ferroelectricity

In 1912, Erwin Schrodinger first coined the term "ferroelectrics" or "ferroelectricity" [8]. Spontaneous polarization in crystalline materials below a specific temperature known as the Curie temperature (Tc) is a phenomenon known as ferroelectricity. Under the influence of an external electric field, the polarization can reverse itself. Ferroelectricity is a spontaneous polarization of the specimen that is electrically switchable. The substances that exhibit this kind of behavior are known as ferroelectric substances or ferroelectrics. Piezo- and pyroelectric properties are shared by all ferroelectric materials. Polarization–electric field (P-E) loop or ferroelectric hysteresis loop are terms used to describe how electric polarization lags behind an



**Fig. 11** Illustration of the pyroelectric effect mechanism

external electric field [110, 111]. However, when an electric field is applied, the crystal's domains have a natural tendency to align in the direction of the field. This results in the manifestation of various phenomena related to the hysteresis loop, including domain rotation and domain growth. Figure 12 illustrates a ferroelectric hysteresis loop. Electric dipoles begin to align themselves towards the electric field when it is applied, which results in net polarization in the specimen. At higher electric fields, every single dipole is pointed directly in the direction of the field, causing saturation in the polarization, also known as saturation polarization ($P_s$) [112, 113]. Polarization changes its direction in response to an electric field reversal. Remnant polarization ($P_r$), a specific value of polarization, exists when the electric field is zero or when there is no electric field. The coercive field ($E_c$) is the name given to the field that is applied in the opposite direction to cause remnant

polarization to be zero. The thickness of the specimen, the locations of flaws, mechanical stress, and thermal treatment are only a few of the variables that might affect the P-E loop. The transition from ferroelectric to paraelectric above Tc reveals the lack of the P-E hysteresis loop [114, 115]. The synthesis and characterization of lead-free materials with properties comparable to those of materials based on $Pb(Zr,Ti)O_3$ (PZT) are receiving a lot of attention in the field of ferroelectrics [116]. When the randomly distributed ferroelectric domains in ferroelectric ceramics are aligned through the poling process, piezoelectricity is produced [117]. During World War II, there was another research that led to the finding of ferroelectricity in barium titanate and other perovskite-based materials [118, 119]. Since then, these materials have been utilized in a wide variety of applications, including the creation of ferroelectric capacitors for electronic devices and non-volatile memory



Fig. 12 **a** Various energy applications like sensors, nanogenerators, and multi-layer capacitors. **b** Understanding ferroelectric behavior: hysteresis loop of polarization (P) versus applied field (E) (copyright permission and copyright clearance center license number 5030130645203)

(FeRAM), piezoelectric sensors, actuators, and even medical ultrasonic imaging. With the help of the tolerance factor (t′), we can describe the ferroelectric behavior of perovskites. Anti-ferroelectrics have a distribution of $0.78 \le t' \le 1.0$, while ferroelectrics cover the whole perovskite range of $0.78 \le t' \le 1.05$. Halliyal and Shrout found that plotting $t$ versus the average electro-negativity as expressed by [120]

$$\lambda = (\mu AO + \mu BO)/2 \qquad (4)$$

where $\mu_{AO}$ is the electro-negativity difference between $A$ and $O$. The designations $A$ and $B$ represent cations, while $O$ signifies oxygen. In complex and simple perovskites, phase compounds with low $t'$ and $x$ tended to form pyrochlore phase(s). However, raising $t'$ in solid solutions stabilizes perovskites [121]. Ferroelectrics have a dielectric constant that is two orders of magnitude higher than that of regular dielectrics. $BaTiO_3$, a ferroelectric material with a relative dielectric constant exceeding 2000 and a permanent electric dipole, is an example of this [122]. However, polarization in the solid is caused by the alignment of neighboring unit cell dipoles. The existence of spontaneous polarization promotes numerous energy applications like nanogenerators, sensors, and multi-layer capacitors, as shown in Fig. 11.

## Superconductivity

Superconductivity, a fascinating phenomenon in the field of condensed matter physics, has found intriguing expression in perovskite materials. In recent years, these materials have received considerable attention due to their extraordinary electrical and optical properties, which make them valuable for a variety of applications, ranging from photovoltaics to superconductivity. A superconductor is a material that exhibits zero electrical resistance and expulsion of the magnetic flux when a material is cooled below some temperature (critical temperature). It was first discovered in 1911 by Dutch physicist Heike Kamerlingh Onnes in mercury when he cooled it to 4 °K. Following the discovery of superconductivity in perovskite and related cuprate systems in 1986, interest in the perovskite structure increased dramatically [123]. The intriguing consequences of his renewed interest in perovskites were observations that the structure could accommodate significant levels of $CO_3^{2-}$ on the B cation site, such as the layered perovskites $Ba_{2-x}Sr_xCuO_2CO_3$ [124, 125]. The majority of cuprate superconductors originate from the perovskite structure. In fact, because of its intriguing features, which go beyond superconductivity, perovskite structure compounds are among the most investigated types of compounds currently. Generally, perovskites are defined as $ABX_3$ compounds, where $X$ can be either an oxygen halide or an alkaline earth element, $B$ can be a transition metal element, and $A$ is typically an alkaline earth or rare earth element [126]. Two significant non-cuprate

oxide superconductors, $BaPb_{1-x}BixO_3$ ($T_{c\text{-max}} = 13$ K) and $Ba_{1-x}K_xBiO_3$ ($T_{c\text{-max}} = 30$ K), are derived from $BaBiO_3$ with the $ABX_3$ perovskite structure [127, 128]. The structural foundation for supporting charge density waves (CDWs) in $BaBiO_3$ and a combination of $Bi^{3+}$ and $Bi^{5+}$ is provided by this crystal structure [129–131]. The phenomenon of superconductivity can be easily explained by the BCS theory, which is based on the Cooper pair. A Cooper pair is an electron–electron pair that is formed at low temperatures. Numerous practical applications have resulted from these properties, including highly efficient electrical transmission lines, powerful electromagnets used in magnetic resonance imaging (MRI) devices, and particle accelerators. Table 3 illustrates the composite of a superconductor with its critical temperature and critical pressure. At the starting stage, the critical temperature is very low for the superconductor materials.

$$K * T = 1.3\text{hw}D/2 \prod e1/[N(E_F) \qquad (5)$$

Mixed valence oxides have a low tendency of states per unit cell $N(E_F)$ at the Fermi level and should have a tendency of large electron–phonon coupling constant $V^*$.

The phase diagram of coupling constant $\lambda = [N(E_F)] V^*$ versus $T$ proposed by Chakraverty has three phases: metallic, insulating bipolaronic, and superconductor. Metallic has a small value of $\lambda$, insulating bipolaronic has a large $\lambda$, and superconductors have $\lambda$ between both, as shown in Fig. 13a. The Jahn–Teller (JT) polaron model is the primary source of knowledge regarding the increase in critical temperature. This model proposes that a nonlinear molecule or molecular complex that exhibits electronic degeneracy will inherently endure distortion in order to eradicate or mitigate this degeneracy. In cases of minor JT disorder in which the stabilization energy (EJT) remains less than the metal's bandwidth, an increase in EJT corresponds to a greater propensity for localization. These electron and lattice distortion combinations, characterized by a substantial effective mass, are capable of traversing the lattice as a single unit. As a result, a strong electron–phonon coupling becomes evident. Hence, cuprates are introduced in making superconductors, which are helpful in raising the critical temperature. Figure 13b shows the increase in critical temperature with respect to the year of discovery in cuprates. The cuprate superconductor adopts the structure of perovskites, in which electron moves within weakly coupled copper oxide ($CuO_2$) with strain-tuning effect in perovskite [143].

## Applications

Perovskite having different properties relates to different types of applications. The main reason behind their different properties is because of their crystal structure. On the basis

**Table 3** Composite of superconductor with their critical temperature and critical pressure

| S. no | Compositions | Critical pressure | Critical temperature | Ref |
|---|---|---|---|---|
| 1 | $YBa_2Cu_3O_{7-x}$ | 0.62 GPa | 93 K | [132] |
| 2 | $HgBa_2Ca_{2-x}La_xCu_3O_{8+\delta})$ | 0.62 GPa | 93 K | [132] |
| 3 | $(Cu_{0.5}Tl_{0.5})$ $Ba_2Ca_2Cu_3O_{10-\delta}$ (CuTl-1223) | 0.202 GPa | 96 K | [133] |
| 4 | $(Ag)x/CuTl-1223$ | 0.202 GPa | 99 to 107 K | [134] |
| 5 | $Ba_{1-x}K_xSbO_3$ | 12 GPa | 30 K | [135] |
| 6 | $K_3C_{60}$ | Less than 0.3 GPa | 18 K | [136] |
| 7 | $Cr_3RhN$ | – | 17 K | [137] |
| 8 | $Ti_2Ba_2Ca_2Cu_3O_{10-x}$ | 7 GPa | 131.8 K | [138] |
| 9 | $MgCNi_3$ | 25 GPa | $\approx 7.6$ K | [139] |
| 10 | $Ba(Pb_{1-x}Bi_x)O_3$ | 1 atm = 101,325 Pascal | 13 K | [140] |
| 11 | $La_{2-x}Sr_xCuO_{4-y}$ | – | 39 K | [141] |
| 12 | $YRh_3B_{1-x}$ | – | 0.65 K | [142] |

of their multifunctional properties, perovskite materials can be used for different applications, as discussed below.

## Solar cell

The combination of two terms, photo and voltaic, illustrates the process of conversion. Photovoltaics convert solar energy into electrical power. Photo means light, and voltaic means electricity. We used cells, which are mostly made of silicon, the most prevalent element, for them to function. Numerous materials have already been published in the past, leading to different generations of solar cells. There are essentially three generations of solar cells. Using both mono- and polycrystalline $SiO_2$, the first generation of solar cells had a power conversion efficiency (PCE) of roughly 25%. The second generation of semiconductors included amorphous $SiO_2$ and a variety of semiconductor materials, such as gallium arsenide (GaAs), cadmium telluride (CdTe), and copper indium gallium selenide (CIGS). The potential productivity of these cells is close to 20%. A new generation of solar cells was introduced because, despite their extreme PCEs, the first generation of solar cells was costly, the second generation was toxic, and there was a shortage of materials [61]. Thus, the primary goal of the third generation of solar cells is to create more environmentally friendly, more affordable, and more solar energy-producing solar cells than the previous generation. Consequently, the scientists focused their attention on third-generation solar cells, which are essentially made of polymers and a variety of particular micro- and nanomaterials [144]. The third generation of solar cells is perovskite. Perovskite solar cells (PSCs) have garnered significant interest owing to their exceptional power conversion efficiency (PCE) attained in a very short duration and remarkably low material expenses. PSCs utilize organic–inorganic metal halide perovskites as the active

layer in photovoltaic devices [145]. Further reports in 2014 revealed a PCE of 19.3% and a certified PCE of 17.9%, following the initial report in 2012 on a long-term, durable solid-state perovskite solar cell with a PCE of 9.7% [146]. In the last few years, the power conversion efficiency of PSCs has rapidly increased from 3.8 [147] to 22.1% [148], outperforming the well-researched dye-sensitized solar cells (DSSC) and organic photovoltaics (OPV), as well as competing with well-established photovoltaic technologies based on Si, GaAs, and copper indium gallium selenide (CIGS). As one of the "Top 10 Emerging Technologies of 2016," perovskite photovoltaic is currently thought to be the most promising photovoltaic technology for the upcoming generation of solar cells [149]. The chemical formula for the metal halide perovskites is $ABX_3$, where X is a halide anion (such as $Cl^-$, $Br^-$, and $I^-$) and A is typically a monovalent organic or inorganic cation. Formamidinium ($[HC(NH_2)^+]$) and methylammonium ($CH_3NH_3^+$) are examples of organic cations that can occupy the A site. Inorganic cations that can occupy the A site include $Cs^+$. A tunable band gap, a high absorption coefficient, an ambipolar carrier transport property, long carrier diffusion lengths [150], a high defect tolerance, and more are found to be characteristics of the hybrid perovskites, which make it an ideal light absorber. The n-type electron collector and p-type hole collector layers are sandwiched between perovskites, which act as an absorbing layer [151]. The fill factor (FF), open circuit voltage ($V_{oc}$), and other cell parameters are largely controlled by each of these layers. Figure 14 shows the schematic diagram of the perovskite solar cell. The process of making perovskite solar cells (PSCs) is sequential. An electron transport layer, a perovskite transport layer, and a hole transport layer on an FTO or glass substrate make up the basic PSC. Mesoporous titanium dioxide is deposited as the initial step over a transparent substrate in a manner similar to that of

**Fig. 13** **a** Electron–phonon coupling constant with temperature and **b** increase in critical temperature with respect to the year of discovery in cuprates
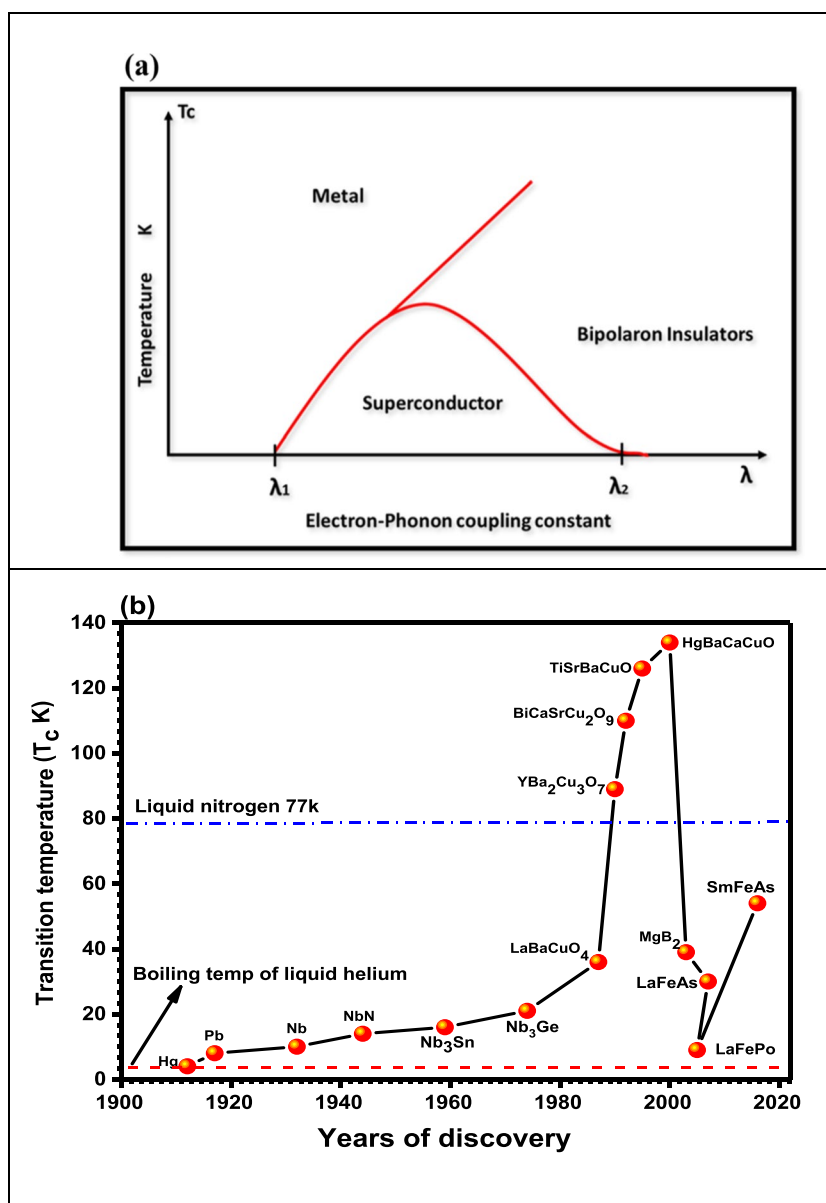
an electron transport layer (ETL). There are several other inorganic and organic ETLs that have been connected to the PSCs. The ETL must have a higher transmission rate than the perovskite layer in order for the perovskite layer to absorb the excitons. The perovskite film is then deposited over the ETL. On the ETL and hole transport layer (HTL) sides, respectively, low- and high-work-function electrodes can be used. A perovskite absorber prevents charge recombination by having a balanced diffusion length of electron and hole of greater than 500 nm [152, 153]. A high recombination rate is caused by electron and hole clouding in the device architecture. By providing a suitable path for both electrons and holes in a planar heterojunction PSC, the PCE can be significantly enhanced. Finding the right precursor concentration in the right solvent, as well as controlling the crystallization time and temperature, is a key factor in attaining optimal solar cell performance. Another important factor is the thickness of the perovskite films [154, 155]. Fundamental research in the field of photovoltaic perovskites is accelerating. A literature survey conducted in 2012 with the term "perovskite-based solar cells" in the heading produced about 7 results; however, by 2023, that number had increased to 1760. Due to intense efforts, the PCEs of PSCs have increased from 9.7 to 25.2% in just 9 years. Perovskite solar cells are anticipated to be a competitive alternative to $SiO_2$-dependent solar cells in the upcoming years [156]. The studied materials for perovskite solar cells are $CH_3NH_3PbI_3$, $CH_3NH_3PbI_{3-x}Cl_x$, $CH_3NH_3PbBr_3$, $CH_3NH_3Pb(I_{1-x}Br_x)_3$, $HC(NH_2)_2PbI_3$, $HC(NH_2)_2Pb(I_{1-x}Br_x)_3$, and $CH_3NH_3SnI_3$. One can observe that the majority of iodide perovskites

**Fig. 14** Schematic representation of perovskite solar cell. Adapted with permission from reference [157]
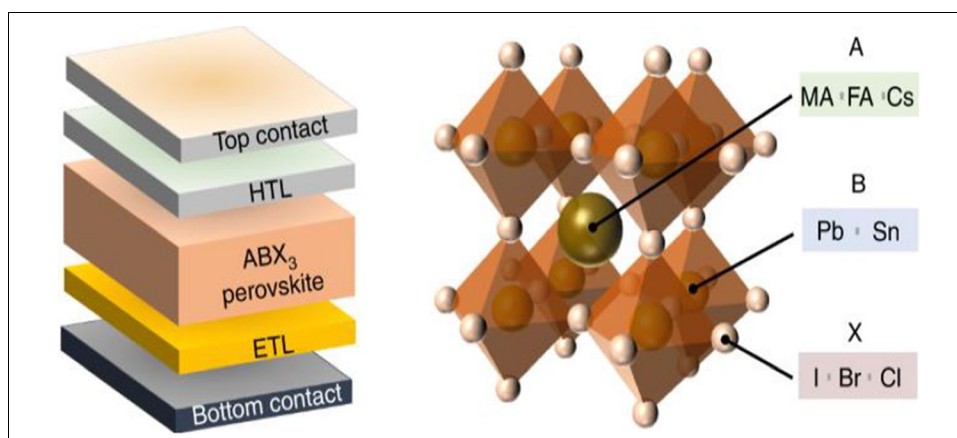


have an open-circuit voltage greater than 1 V and that the voltages of their bromide analogues are higher than those of their iodide counterparts. Because bromide perovskite has a wider band gap than iodide, this is the cause. High-efficiency perovskite solar cells also require HTM materials. The most researched HTM in this regard is spiro-MeOTAD, but polymeric HTMs that have also been tested include the tryarylamine-based PTAA and the thiophene derivative P3HT. Also confirmed to be appropriate for perovskite solar cells are inorganic HTMs like NiO, CuI, and CuSCN [146].

## Solid oxide fuel cells

A fuel cell is an electrochemical device that produces electricity via a chemical reaction between a fuel and an oxidizing agent, typically oxygen or air. It operates on the same fundamental principles as a battery but differs significantly in that it can generate electricity continuously as long as it is supplied with fuel [158, 159]. Fuel cells are one of the most auspicious technologies, and there are various types of fuel cells depending on the nature of the electrolyte used: solid-oxide fuel cell (SOFC), molten carbonate fuel cell (MCFC), polymer electrolyte (proton exchange) membrane fuel cell (PEMFC), phosphoric acid fuel cell (PAFC), direct methanol fuel cell (DMFC), and alkaline fuel cell (AFC) [160]. Particularly, SOFCs have gained much attention in recent years. This increased interest in solid oxide fuel cells is due to the various advantages of SOFCs, among other forms of fuel cells. SOFCs are the technology that can be a driving force to change the course of action in the modern era due to their optimal power generation features and maximum electrical efficiency for automobiles and household devices [161]. Here are some key advantages of SOFCs: high efficiency shown by SOFCs, typically around 60–70%. High-temperature procedure allows for efficient conversion of chemical energy into electricity. SOFCs can run on a wide range of fuels, which include hydrocarbons, natural gases, methane, propane, and hydrogen. SOFCs can also run on

biofuels or a combination of fuels, which provides versatility and adaptability in various sittings [162]. Other benefits include low air pollution and greenhouse gas emissions from high-temperature operation and a long operating lifespan. SOFCs can function at moderate temperatures, making them useful for many applications. SOFCs are considered an exciting option for the future production of clean energy. Unlike conventional heat engines, SOFC technology does not have problems with leakage, lubrication, or heat loss. Perovskite materials are extensively utilized in SOFCs as the cathode, the anode, and the electrolyte. This is due to the fact that large varieties of dopants that have distinct and variable states are readily available and may be positioned at the A and B sites. Figure 15 shows the systematic diagram of SOFCs.

The basic structure of a solid oxide fuel cell typically consists of several key components: electrolyte, anode, cathode, bipolar plates, and current collectors. Cathode: the cathode is the electrode on the oxidant (usually air or oxygen) side of the SOFCs. Perovskite minerals are frequently used in their production; examples include lanthanum strontium manganite (LSM) and lanthanum strontium cobalt ferrite (LSCF). By taking electrons and oxygen ions in order to generate oxide ions, the cathode makes the electrochemical reduction of oxygen easier to accomplish, and the anode is the electrode on the fuel side of the SOFC [163]. In Table 4, we discuss the method of preparation, phase formation, power density, and conductivity of perovskite-based cathode materials for SOFCs.

Porous materials, such as ceramics based on nickel or cermet (ceramic–metal composites), are usually utilized in their construction. The anode acts as a catalyst for the electrochemical oxidation of the fuel, which in this case is hydrogen, into protons and electrons [179]. In Table 5, we discuss the method of preparation, phase formation, power density, and conductivity of perovskite-based anode materials for SOFCs. The electrolyte in the solid oxide fuel cell is an essential component because it serves to partition the fuel and oxidant gases

**Fig. 15** Working diagram of solid oxide fuel cell
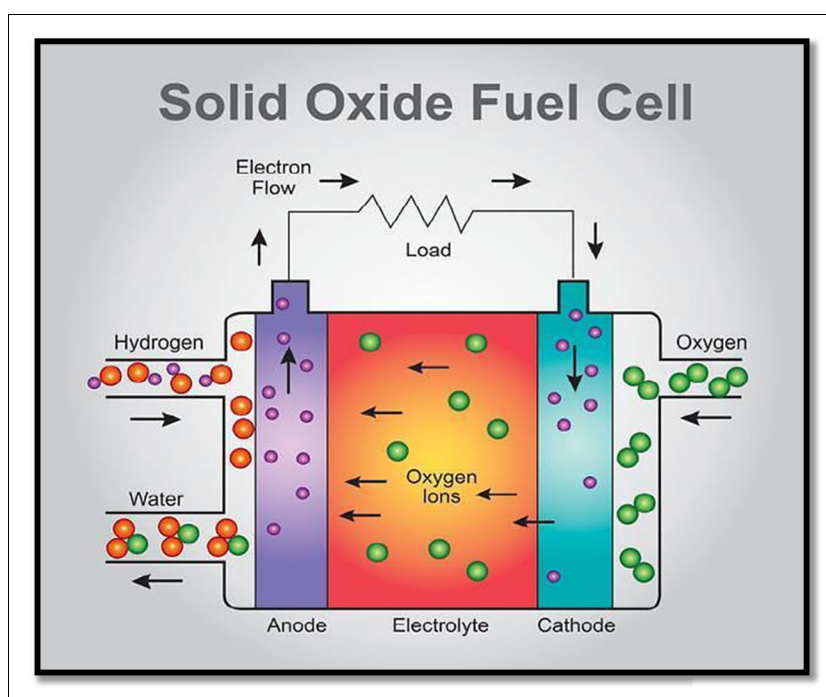


while simultaneously facilitating the movement of oxygen ions. Materials such as yttria-stabilized zirconia (YSZ) and scandia-stabilized zirconia (ScSZ) are examples of materials that are frequently utilized for the electrolyte. The electrolyte material that is used is determined by a number of criteria, including the operating temperature and the performance requirements [180]. In stack designs, bipolar plates are utilized to transport gases and serve as current collectors. These plates are also employed. They are typically constructed out of materials that are resistant to corrosion and feature flow

**Table 4** Perovskite-based cathode materials for SOFCs

| Perovskite cathode materials | Method | Phase | Power density (mW/cm$^2$) | Conductivity (S/cm) | Ref |
|---|---|---|---|---|---|
| $SrFe_{1-x}Mo_xO_3 - 1$ ($x=0.25$) | Microwave-assisted combustion method | Cubic Pm-3m | – | 22 at 800 °C | [164] |
| $Pr1-Ca_xBaCo_x2O_{5+\delta}$ | Solid-state | P4/mmm tetragonal | 646.5 at 800 °C | 320 at 800 °C in air | [165] |
| $SmBaCo_{0.5}Mn_{1.5}O_{5+\delta}$ | Sol–gel method | Tetragonal P4/mmm | 1060 at 900 °C | 33 at 900 °C | [166] |
| $Nd_{0.5}Sr_{0.5}Co_{0.5}Fe_{0.5}O_{3-\delta}$ | Sol–gel method | Cubic Pm-3m | 1560 at 650 °C | – | [167] |
| $GdBaFeNiO_{5+\delta}$ | Sol–gel method | Orthorhombic Pmmm | 515 at 800 °C | 9.5 at 400 °C | [168] |
| $La_{0.35}Pr_{0.15}Sr_{0.5}FeO_{3-\delta}$ | Wet chemical route | Cubic Pm-3m | 1083 at 700 °C | – | [169] |
| $NdBaFe_2\_Mn_xOx_{5+\delta}$ | Sol–gel method | Cubic Pm-3m | 453 at 700 °C | 114 at 550°C in air | [170] |
| $Pr_{0.9}Ca_01-xCa_xCo_2O_{5+\delta}$ ($x=0.2$) | Sol–gel process | Tetragonal P4/mmm | 712 at 800°C | – | [171] |
| $LnBaCoFeO_{5+\delta}$ (Ln = Pr, Nd) | EDTA-citrate complexing method | P4/mmm tetragonal | 749 and 669 at 800 °C | 321 and114 at 350°C | [172] |
| $NdBaCo_{2/3}F_{2/3}Cu_{2/3}O_{5+\delta}$ | EDTA citric acid complexation method | P4/mmm tetragonal | 736 at 800 °C | 92 at 625 °C | [173] |
| $YBa_{0.5}Sr_{0.5}Co_{1.4}Cu_{0.6}O_{5+\delta}$ | Sol–gel method | Orthorhombic | 398 at 850 °C | 174 at 350 °C in air | [174] |
| $Sr_2Fe_{1.5}Mo_{0.5}O_{6-\delta}$ | Combustion method | Pnma orthorhombic | 1102 at 800 °C | 30 at 550 °C | [175] |
| $PrBa_{0.5}Sr_{0.5}Co_{2-x}Fe Ox_{5+\delta}$ ($x=0.56$) | Polymerization method | Pmmm orthorhombic | 97 for at 850 °C | 60 at 850°C | [176] |
| $SrCo_{0.8}Ti_{0.1}Ta_{0.1}O_{3-\delta}$ | Solid-state | – | 1.99, 1.75, 1.28, and 0.90 at 650, 600, 550, and 500 °C | 65–142 at 400–650 °C | [177] |
| $BaFe_{0.95}Pr_{0.05}O_{3-\delta}$ | Sol–gel method | Cubic Pm-3m | 798.7 at 750 °C | 12.6 at 750 C | [178] |

channels that allow for the fuel and oxidant gases to be distributed evenly over the cell surfaces. Current collectors are components that work to collect the electrical current that is produced by the individual cells that make up a stack and then send that current to an external circuit. In most cases, these will be constructed out of conductive materials, and they will be in physical touch with the electrodes [181].

## Thin film capacitors

Perovskite thin films have high dielectric values, which makes them ideally suitable for capacitor applications. Capacitors are generally used for signal coupling, signal decoupling, filtering, and impedance matching. Single-layer thin films have lower inductance than multi-layer ceramic capacitors because of the high mutual inductance between the internal counter electrodes, which can lead to a reduction in the size of electronic systems due to the integration of the capacitor and another component. The reduction of components improves the performance of the system. This aspect is critical for high-frequency circuitry [192]. Thin films designed for employment within the microwave frequency spectrum are coveted due to their inherent attributes, including minimal attenuation at microwave frequencies, negligible intermodulation distortion, and cost-effectiveness in the production process. Moreover, thin-film devices have a distinct advantage over bulk materials because their structural configurations are perfectly compatible with planar microwave circuits [192–194]. The equation of energy density obtained from the polarization–electric field (P-E) relation says the predominant energy storage property can be ascribed to both large dielectric polarization and high breakdown strength [195].

$$U = \int_0^{p_{max}} Edp \qquad (6)$$

"$P_{max}$" and "E" refer to the maximal polarization and breakdown strength, respectively, in this context. In addition, energy loss must be considered when coping with the delay in polarization saturation within P-E loops [195–198]. This factor can have a substantial effect on the energy efficacy of energy storage devices. In general, the energy storage efficacy of thin film samples is significantly superior to that of their bulk counterparts. Thin films with fewer defects can attain higher breakdown strength, which is an advantage. Consider the ferroelectric material $_{0.88}BaTiO_{3-0.12}Bi(Mg_{1/2}Ti_{1/2})O_3$, which has a relaxor-type configuration. This material can withstand an ultrahigh dielectric breakdown strength of 1900 kV/cm in its thin film state, resulting in an energy storage density of up to 37 J/cm$^3$. In contrast, the same composition in its bulk state obtains a relatively lower electric field of 224 kV/cm, resulting in a density of energy storage of 1.81 J/cm$^3$ [197–199]. Because of their extraordinary ultrahigh dielectric breakdown strength, the use of lead-free dielectric ceramics in thin film form is highly recommended for both environmental sustainability and optimum energy storage performance. $SrTiO_3$ films grown on a $La_{0.67}Sr_{0.33}MnO_3$ electrode attained an impressive energy density of approximately 307 J/cm$^3$ with an energy efficiency of approximately 89%. At the interface of $SrTiO_3$ and $La_{0.67}Sr_{0.33}MnO_3$, oxygen vacancies and an ion interdiffusion layer are created, which contributes to this material's exceptional performance [200]. Perovskites and their unique properties, such as high energy conversion efficiency and the ability to be processed as thin films, have garnered considerable attention. Table 6 shows the comparison based on the energy storage density ($W_{rec}$) and efficiency (in %) of some thin films. Notably, Zhai and Shen reported an exceptional energy density of 31.96 J/cm$^3$ and an energy efficiency of 61% at 2400 kV/cm of electric field strength. This accomplishment was made possible by a multi-layered, lead-free $_{0.94}(Bi_{0.5}Na_{0.5})_{0.94}TiO_{3}$-$_{0.06}BaTiO_3/$

**Table 5** Perovskite-type anode materials for SOFCs

| Perovskite anode materials | Method | Phase | Power density (mW/cm$^2$) | Conductivity (S/cm) | Ref |
|---|---|---|---|---|---|
| $A_2FeMoO_{6-\delta}$ ($A$ = Ca, Sr, Ba) | Solid-state method | Monoclinic, tetragonal, cubic | 831 for $A$ = Sr, 561 for $A$ = Ba, and 186 for $A$ = Ca at 850 °C | – | [182] |
| $Sr_2FeTiO_{6-\delta}$ | Ball-milling | Pm-3m cubic | 441 and 335 at 800 °C | 2.83 at 800 °C | [183] |
| $Sr_2Fe_{1.5}Mo_{0.5}O_{6-\delta}$ | Sol–gel | Fm-3m cubic | 42.6 at 800 °C | 59.48 at 800 °C in air | [184] |
| $La_2ZnMnO_6$ | Wet chemical method | P21/n monoclinic | 155 at 650 °C | 0.054 at 650 °C | [185] |
| $Sr_2FeNb_{0.2}Mo_{0.8}O_{6-\delta}$ | Solid-state method | I4/mmm tetragonal | – | 19.5 in air and 5.3 in 5% H$_2$ at 800 °C | [186] |
| Mo-$Pr_{0.5}Ba_{0.5}MnO_{3-\delta}$ | Sol–gel | Cubic and hexagonal | 700 at 850 °C | 101 in air at 800 °C | [187] |
| $SrMo_{1-x}Ga_xO_{3-\delta}$ ($x$ = 0.1) | Wet chemical method | Pm-3m cubic | 900 at 850 °C | 268 at 850 °C | [188] |
| $La_{0.5}Sr_{1.5}Fe_{1.5}Mo_{0.5}O_{6-\delta}$ | Sol–gel | Pm-3m cubic | 1156 at 800 °C | 23 at 800 °C | [189] |
| $PrBaMn_2O_{5+\delta}$ | Pechini method | Cubic and hexagonal | 1.7 at 800 °C | 8.16 800 °C | [190] |
| $SrMo1-xMgxO_3\,\check{}\delta$ ($x$ = 0.1, 0.2) | Soft chemistry procedures | Cubic Pm-3m | 555 and 832 at 850 °C | 146 and 114 at 850 °C | [191] |

BiFeO$_3$ thin film heterostructure with a 4-layer BiFeO$_3$ film. The enhanced insulative properties and dielectric breakdown strength at the interfaces were crucial to this extraordinary performance [201].

## Laser and light-emitting diodes

Lasers and light-emitting diodes (LEDs) are both pivotal light sources in modern technology, yet they differ significantly in terms of operation and application.

- Laser (light amplification by stimulated emission of radiation). Lasers operate using the stimulated emission principle. They produce light that is highly focused, coherent, and monochromatic, meaning that the light waves are in phase, have a single color, and are focused on a narrow beam. This extraordinary precision renders lasers indispensable for a variety of applications, including cutting and welding in manufacturing, medical procedures, and optical communication. Each form of laser, including gas lasers, solid-state lasers, and semiconductor lasers, is designed for a particular function.
- Light-emitting diodes (LEDs). LEDs are semiconductor devices that emit light when an electric current flows through them. LEDs emit incoherent light with a broader spectrum of colors than lasers. LEDs are extensively employed in numerous applications, including display screens, indicator lights, streetlights, and residential lighting. Compared to traditional incandescent bulbs, they have a longer lifespan and utilize considerably less energy. Organic LEDs (OLEDs) and quantum dot LEDs, which were made by advancements in LED technology, offer even greater versatility and color accuracy. However, it is essential to note that the commercialization of perovskite-based lasers and LEDs is an ongoing area of research, and challenges related to stability and longevity need to be addressed before they can be widely adopted in practical applications. Researchers are actively working to overcome these hurdles to unlock the full potential

of perovskite materials in laser and LED technologies. In order to satisfy the requirements of the detailed balancing equation, it is essential to have an external luminescence efficiency that approaches 100%. This condition is a fundamental necessity for attaining the Shockley-Queisser limit, which is an estimated efficiency of 33.5% in solar cells. This highlights the necessity for a solar-cell material of outstanding quality that not only has amazing photovoltaic characteristics but also serves as an extraordinary light emitter. Since their introduction in the mid-twentieth century, semiconductor solid-state lasers have seen significant advancements and have become ubiquitous elements in our everyday lives. In the present scenario, solution-processed gain media, such as organic polymers and colloidal quantum dots, have emerged as viable alternatives with potential. The attraction of these entities arises from their ability to engage in cost-effective and sustainable manufacturing processes, in addition to their compatibility with the seamless incorporation of adaptable and wearable optoelectronic devices. The amplified spontaneous emission/lasing from perovskite materials is shown in Table 7. An important development in this field is the rise of halide perovskites, which has established them as viable competitors in the field.

## Non-volatile memories

There are several memory architectures available that meet the growing need for next-generation non-volatile memory devices with faster switching speeds and greater endurance, such as resistive switching random access memory (ReRAM) [215], magnetic random access memory (MRAM) [216], and phase-change random access memory (PRAM) [217]. Non-volatile memories are an important part of computer components. These materials can retain the information within the material itself when the power is interrupted. In developing non-volatile memories, there has been the use of ferroelectric thin films (ferroelectric random-access memories or Fe-RAMs). In Fe-RAMs, information is stored in the polarization state of the material. Early work was focused on PZT and SBT. In films, there must be a large difference between these two characteristics: remnant polarization ($P_r$) and reliable polarization cycling [193, 194]. One of the new storage devices for managing mass data is RRAM. Resistive random-access memory is promising because of its simple structure, fast switching, low power consumption, and high density. RRAM stores data through current-stage changes under electric fields. Active layers can be electrically charged from a low resistance state (LHS) to a high resistance state (HRS) by applying voltages at different amplitudes [218]. RRAM has a sandwich-like structure

**Table 6** Comparison based on the energy storage density ($W_{rec}$) and efficiency (in %) of some thin films

| Composition | $W_{rec}$ (J/cm$^3$) | Efficiency (%) | Ref |
|---|---|---|---|
| BNKT-0.10BFO | 22.12 | 60.85 | [202] |
| BNKT-15SZ | 34.69 | 59.32 | [203] |
| BiMg$_{0.5}$Ti$_{0.5}$O$_3$ | 26 | – | [204] |
| BiAlO$_3$ | 31.1 | 82.2 | [205] |
| NBT | 12 | 43 | [206] |
| Mn-doped SrTiO$_3$ | 23.8 | 69.8 | [207] |
| BF-KNMN | 28.0 | 90.3 | [208] |
| 0.89NBT-0.06BT-0.05BFO | 42.9 | 65.7 | [209] |

**Table 7** Amplified spontaneous emission from perovskite materials

| Material ($X$=Cl–, Br–, or I–) | Morphology | Pump source S.E | Wavelength (nm) | Modal gain coefficient (cm$^{-1}$) | Threshold (ASE or lasing) (µJ cm$^{-2}$) | Cavity type | Ref |
|---|---|---|---|---|---|---|---|
| $CH_3NH_3PbX_3$ | Thin film | 600 nm, 150 fs | ≈500–790 | 40 | ≈12 (ASE) | N.A | [210] |
| $CH_3NH_3PbI_3$ | Thin film | 530 nm, 4 ns | ≈780 | – | ≈10 (ASE) | N.A | [211] |
| $CH_3NH_3PbI_3$ | Thin film | 532, 1 ns | ≈780 | – | ≈0.32 (lasing) | DFB | [212] |
| $CH_3NH_3PbI_3$ | Microcrystal networks | 355 nm, 0.8 ns | ≈765 | – | ≈200 (lasing) | Random lasing | [213] |
| $CsPbX_3$ | NPs | 400 nm, 100 fs | ≈470–640 | ≈450 | ≈5 − 22 (ASE) | N.A | [214] |

of three layers, which consist of the top electrode, active layer, and bottom electrode. Many material systems exhibit resistive switching behaviors; organics [219, 220], transition metal oxides [221], and perovskite oxides [222] are a few examples. In addition to their hysteretic current–voltage (I-V) responses, analogue switching, flexibility, multilevel data storage, and the potential for low power consumption/ high-density memory applications are some of the benefits of using organic–inorganic hybrid perovskites (OIHPs). Consequently, they have been employed in the production of synaptic and resistive memory devices [223, 224]. For resistive switching memory and other next-generation memory devices, OIHP materials are attractive options for two reasons. Initially, both inorganic and organic counterparts can provide benefits for OIHP. Given that this material contains inorganic components, such as oxides and chalcogenides, it may exhibit superior resistive switching properties. But because of their brittleness, inorganic materials are not as useful for flexible electronics. As a result of the structural flexibility of organic parts, materials like A-site organic cations can find new uses in flexible devices [225]. Secondly, optical memories could potentially use OIHP. Fast optical signal transfer is becoming a major concern in the field of optical communication in order to develop photon-writing memories. The light-harvesting and light-responsive qualities of this material have accelerated the development of photosensory devices, such as photodiodes and phototransistors [226]. A blend of perovskite/PS has been used to demonstrate OIHP-based photo memory with a heterojunction floating gate [227]. Figure 16 shows the schematic illustration of a memory device with an Au/MABI/ITO structure.

In the active layer, there are many materials that can be used, like perovskites, polymers, and oxides [229]. SrZrO$_3$ (SZO) films are examples of a category of perovskite materials in which various dopants can significantly impact the presence of oxygen vacancies and defect levels inside the perovskite switching layers. As a result, these alterations have a noticeable effect on the material's switching characteristics. The primary objective of this study is to examine the effects of co-doping with vanadium (V) and thulium (Tm) on SZO films prepared using the sol–gel

technique [230]. In our literature work, we examine resistance switching in thulium (Tm) and vanadium (V) co-doped SrZrO$_3$ (SZO) films. Sol–gel-synthesized films were merged between oriented Al top and LaNiO$_3$ (LNO) bottom electrodes. The baseline condition is that leakage current density grows proportionally to bias voltage in the first stage. After that, when the top electrode (TE) is given a negative bias voltage greater than − 12 V, leakage current density increases significantly, indicating a high leakage state. After the previous phase, when the tunnelling electrode (TE) is exposed to a positive bias voltage over 10 V, the leakage current density sharply decreases, resulting in a transition into the low leakage state. After surpassing − 10 V, the leakage current density suddenly returns to H-state levels. The device transitions between the high (H-state) and low (L-state) states without returning to the beginning condition during electrical operations, which is known as hysteresis. The leakage states do not change spontaneously without electrical power, and the resistance ratio between them is approximately 10$^4$. The transition between these states is thought to be caused by the formation and destruction of conductivity-promoting channels or filaments [230–235].
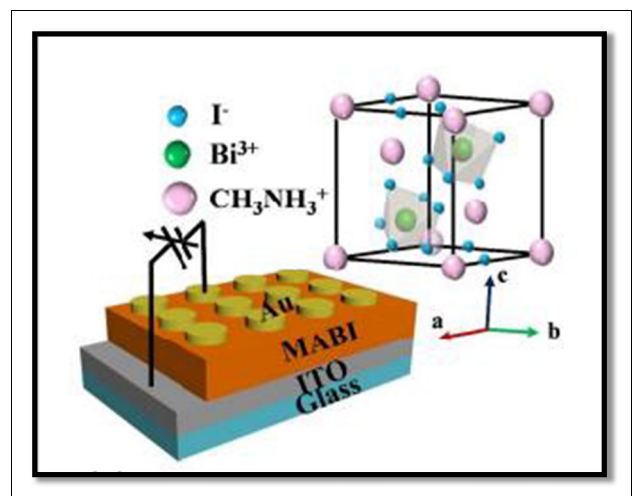


**Fig. 16** Schematic illustration of a memory device with an Au/MABI/ITO structure. Adapted with permission from reference [228]

Figure 17a analyzes the Schottky emission mode: Ln(J) vs. $V^{(1/2)}$ with fitted experimental data (solid line) [236]. The conduction mechanisms of the H-state and L-state were reported to be ohmic conduction and Poole–Frenkel (PF) emission [235]. The repeatable resistance-switching phenomena that are seen can be attributed to the formation of conducting filaments consisting of metallic components. A suitable negative bias stimulates the device's metallic components to form conductive channels. This causes the initial leaking state to change to the high leakage state (H-state). However, a proper positive bias interrupts these conductive channels, returning them to the low leakage state. Vanadium (V) and thulium (Tm) doping significantly affect the operating voltage of the doped $SrZrO_3$ (SZO) system, suggesting device improvement. Figure 17b depicts the effect of the pulse width with a 15 V pulse amplitude on the resistance switching.

A − 15 V with a 5 ns voltage pulse causes a rapid change from the starting condition to the high leaking state (H-state), indicating that the forming process is fast. To analyze the temporal features of the switching dynamics between the H-state and the low leakage state (L-state), negative and positive direct current (dc) voltages are used to produce these states. The high state (H-state) transitions to the low state (L-state) using a 15 V, 5 μs voltage pulse. This pulse triggers a switching process from 500 ns to 5 μs. As pulse width rises, the current density associated with the high state (H-state) decreases before resistance switching. However, a 5 ns voltage pulse from − 15 V converts the L-state to the H-state. Note that the time required to transition from the H-state to the L-state is much longer than the opposite transfer. This shows an imbalance in switching characteristics. The investigation examines how stress duration affects leakage current modification, particularly with varying pulse lengths [230]. The decay of leakage current amplifies as the pulse width diminishes, post-transitioning the leakage state from L-state to H-state via a voltage pulse. Upon employing a − 12 V, 50 μs voltage pulse for the switch, the leakage current remains largely unaltered following 1200 s of 3 V stress. However, when transitioning to the H-state using a − 12 V, 5 ns voltage pulse, the leakage current experiences an approximate 80% decay from its initial magnitude. This decay arises from the formation of unstable conducting paths at smaller pulse widths, which subsequently fracture during voltage stress, leading to a decline in leakage current. Consequently, resistance switching via narrower pulse widths is associated with a more pronounced decay in leakage current. The study also provides insights into the relationship between normalized leakage current and stress time across various stress voltages [230]. When transitioning to the H-state using a − 12 V, 5 ns voltage pulse, it is observed that the decay under a 3 V voltage stress is considerably more pronounced than the decay under a − 3 V stress. In simpler terms, significant decay takes place when the direction of the voltage stress is opposite to that of the initial voltage pulse.

## Future perspectives

Perovskite materials provide an essential family of materials with extraordinarily versatile structural, electric, and optoelectronic properties. Enormous efforts have been made by various researchers to explore $ABO_3$ perovskite symmetry by playing with a variety of cations at the A and B sites. Perovskite materials, with their diverse and unique properties, are suitable for a wide range of applications. These include thin film capacitors, lasers, light-emitting diodes, non-volatile memories, actuators, and sensors. They are also used in various piezoelectric, ultrasonic, and underwater devices, high-temperature heating applications, and frequency filters for wireless communications. Although significant advancement has been made, there are still a large number of derivatives for novel perovskite materials that are theoretically anticipated



**Fig. 17** **A** I–V characteristics of Al/(V:Tm:SZO)/LNO structure—investigating electrical behavior and **b** the plot of leakage current density with a pulse width (copyright permission and copyright clearance center license number 0022–3727)
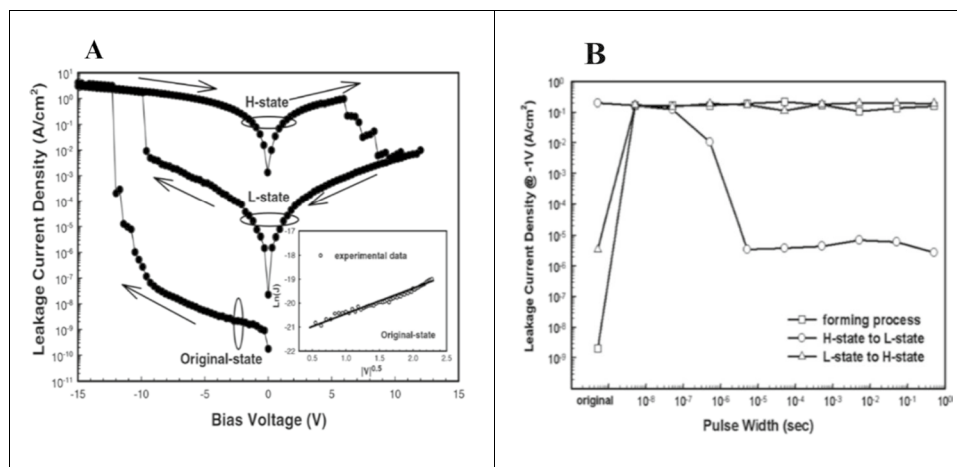
to exist in the future due to their structural and compositional flexibility. Future research must concentrate on discovering more efficient cathodes and anodes for direct hydrocarbon at relatively low temperatures, and these materials must have excellent electrical conductivity and high-temperature stability. SOFC is a device with a solid–solid and gas–solid interface that must be long-lastingly stable at elevated temperatures. In addition, advancements can be made in the areas of synthesizing and designing these materials to improve their piezoelectric and dielectric properties with greater temperature stability. Due to their multi-faceted and versatile properties, many promising candidates of perovskite materials hold great potential to be an integral part of the future developments of miniaturized electronic devices. Though significant progress has been achieved, the development of efficient synthesis and preparation of perovskite nanostructures still remains a huge challenge. This parameter is crucially important to facilitate superior integrated devices for commercialization and become the strategic technologies of the future.

## Conclusion

In this review article, we explain the comprehensive advancements in perovskite materials, underscoring their multifaceted properties and significant impact on energy harvesting applications. Perovskites, with their adaptable ABO3 structure, have emerged as a cornerstone in the field of materials science, offering a broad spectrum of electrical, optical, and mechanical properties. Their versatility extends from solar cells with unprecedented efficiency levels to applications in LEDs, sensors, and actuators, manifesting a revolution in renewable energy technologies and electronic devices. The exploration of lead-free perovskites and the quest for environmentally benign alternatives underscore the commitment to sustainable development within the field. As research continues to push the boundaries of what is possible with perovskite materials, the potential for innovation remains boundless, promising to usher in a new era of technological advancements that are sustainable, efficient, and transformative. This review not only highlights the significant strides made in understanding and harnessing the properties of perovskites but also sets the stage for future research directions that could further amplify the impact of these materials on various technological domains.

**Author contribution** Sahil Kumar: Writing—original draft preparation. Neha Kumari: review and methodology. Vishal Sharma: figure preparation and writing. Gun Anit Kaur: investigation. Anirban Saha: editing. Sapna Thakur: software and validation. Mamta Shandilya: supervision and reviewing.

**Data availability** No datasets were generated or analyzed during the current study.

## Declarations

**Ethics approval** This declaration is not applicable.

**Competing interests** The authors declare no competing interests.

The manuscript has not been published elsewhere, is not under editorial review for publication elsewhere, and is not being submitted simultaneously to another journal.

## References

1. Cheng Z, Lin J (2010) Layered organic–inorganic hybrid perovskites: structure, optical properties, film preparation, patterning and templating engineering. CrystEngComm 12(10):2646–2662
2. Muller O, Roy R (1974) The major ternary structural families. Springer Verlag, Berlin, Heidelberg, and New York (T974. ix+487 pp., 46D M 76, US)
3. Barbieri F et al (2023) On the structural, optical and polarization properties of the incipient ferroelectric $CaTiO_3$ compound. Ferroelectrics 611(1):279–286
4. Curie J, Curie P (1880) Development by pressure of polar electricity in hemihedral crystals with inclined faces. Bull soc min de France 3:90
5. Kumar S et al (2023) Efficacy of polymeric nanofibrous membranes for proficient wastewater treatment. Polym Bull 80(7):7145–7200
6. Matthias B, Von Hippel A (1948) Domain structure and dielectric response of barium titanate single crystals. Phys Rev 73(11):1378
7. Kaur GA, Kumar S, Shandilya M (2020) Fabrication of piezoelectric nanogenerator based on P (VDF-HFP) electrospun nanofiber mat-impregnated lead-free BCZT nanofillers. J Mater Sci Mater Electron 31(22):20303–20314
8. Busch G (1987) Early history of ferroelectricity. Ferroelectrics 74(1):267–284
9. Guleria G et al (2023) Biomedical potential of hydrothermally synthesized zinc oxide nanoparticles for antifungal evaluation and cytotoxicity analysis. Appl Organomet Chem 37(12):e7270
10. Kwon OD et al (2005) A research on the piezoelectric vibration actuator for mobile phone. In: Proceedings of 2005 international symposium on electrical insulating materials, 2005. (ISEIM 2005), vol 3. IEEE
11. Rice C et al (1988) Preparation of superconducting thin films of calcium strontium bismuth copper oxides by coevaporation. Appl Phys Lett 52(21):1828–1830
12. Shandilya M et al (2017) Effect of addition of zinc ferrite on dielectric and magnetic properties of (Ba, Ca) $TiO_3$ ceramics. Integr Ferroelectr 185(1):147–154
13. Kumar D et al (2022) A very low temperature growth of $BaTiO_3$ nanoparticles by sol-hydrothermal method. Phys Status Solidi A 219(23):2200238
14. Rana G et al (2022) Investigation of structural and morphological properties of BaZr0. 10Ti0. 90O3/$Ga_2O_3$ nanostructures. In: AIP conference proceedings, vol 2357. No 1. AIP Publishing
15. Merz WJ (1950) The effect of hydrostatic pressure on the Curie point of barium titanate single crystals. Phys Rev 78(1):52

16. Samara G (1971) Pressure and temperature dependence of the dielectric properties and phase transitions of the ferroelectric perovskites: PbTiO3 and BaTiO3. Ferroelectrics 2(1):277–289

17. Bai Y et al (2017) Ferroelectric, pyroelectric, and piezoelectric properties of a photovoltaic perovskite oxide. Appl Phys Lett 110(6):063903

18. Maeno Y et al (1994) Superconductivity in a layered perovskite without copper. Nature 372(6506):532–534

19. Zhao TL et al (2019) Giant piezoelectricity of ternary perovskite ceramics at high temperatures. Adv Func Mater 29(12):1807920

20. Hu Q et al (2023) Boosting the piezoelectric property of relaxor ferroelectric single crystal via active manipulation of defect dipole polarization. J Materiomics 9(1):166–173

21. Wang M et al (2021) Lead-free perovskite materials for solar cells. Nano-Micro Letters 13:1–36

22. Rojac T (2023) Piezoelectric response of disordered lead-based relaxor ferroelectrics. Commun Mater 4(1):12

23. Li F et al (2016) The origin of ultrahigh piezoelectricity in relaxor-ferroelectric solid solution crystals. Nat Commun 7(1):13807

24. Fan P et al (2019) Large strain under low driving field in lead-free relaxor/ferroelectric composite ceramics. J Am Ceram Soc 102(7):4113–4126

25. Mitzi DB (2019) Introduction: perovskites. Chem Rev 119(5): 3033–3035

26. Moure C, Peña O (2015) Recent advances in perovskites: processing and properties. Prog Solid State Chem 43(4):123–148

27. Bhalla A, Guo R, Roy R (2000) The perovskite structure—a review of its role in ceramic science and technology. Mater Res Innovations 4(1):3–26

28. Wentzcovitch R et al (1998) High pressure elastic anisotropy of MgSiO3 perovskite and geophysical implications. Earth Planet Sci Lett 164(1–2):371–378

29. Shandilya M et al (2017) Modification of structural and electrical properties of ca element on barium titanate nano-material synthesized by hydrothermal method. Ferroelectrics 520(1):93–109

30. Glazer AM (1972) The classification of tilted octahedra in perovskites. Acta Crystallogr Sect B: Struct Crystallogr Cryst Chem 28(11):3384–3392

31. Ning W, Gao F (2019) Structural and functional diversity in lead-free halide perovskite materials. Adv Mater 31(22):1900326

32. Whitfield P et al (2016) Structures, phase transitions and tricritical behavior of the hybrid perovskite methyl ammonium lead iodide. Sci Rep 6(1):35685

33. Wei W-J et al (2019) Phase transition, optical and dielectric properties regulated by anion-substitution in a homologous series of 2D hybrid organic–inorganic perovskites. J Mater Chem C 7(38):11964–11971

34. Kumar S et al (2023) Optical coalition in the electrical and magnetic induction of Dy and Tb-doped BFO-based multiferroic. Appl Phys A 129(1):21

35. Kostopoulou A et al (2019) Perovskite nanocrystals for energy conversion and storage. Nanophotonics 8(10):1607–1640

36. Rana P et al (2022) Recent progress in piezoelectric properties of lead-free perovskite sodium potassium niobate. AIP conference proceedings, vol 2357, No. 1. AIP Publishing

37. Graetzel M, Park NG (2014) Organometal halide perovskite photovoltaics: a diamond in the rough. Nano 9(05):1440002

38. Mukherjee B, Fedorova NS, Íñiguez-González J (2024) First-principles predictions of HfO $_2$ $-based ferroelectric superlattices. arXiv preprint arXiv:240105288

39. Maity K, Mandal D (2021) Piezoelectric polymers and composites for multifunctional materials. In: Advanced lightweight multifunctional materials. Woodhead Publishing, pp 239–282

40. Kaur GA et al (2023) Enhancement in the dielectric and ferroelectric behaviour by interface between the electrode and grain bulk boundaries of Ca, Zr-doped barium titanate. Inorg Chem Commun 151:110644

41. Maier R et al (2015) Acceptor-oxygen vacancy defect dipoles and fully coordinated defect centers in a ferroelectric perovskite lattice: electron paramagnetic resonance analysis of Mn2+ in single crystal BaTiO3. J Appl Phys 118(16):164102

42. Navrotsky A (1998) Energetics and crystal chemical systematics among ilmenite, lithium niobate, and perovskite structures. Chem Mater 10(10):2787–2793

43. Grundmann M (2010) Physics of semiconductors, vol 11. Springer. https://doi.org/10.1007/978-3-030-51569-0

44. Yang Y et al (2006) Photoinduced structural transformation of SrFeO3 and Ca2Fe2O5 during photodegradation of methyl orange. Mater Sci Eng B 132(3):311–314

45. Eiselt L et al (2023) Hole-doped high entropy ferrites: structure and charge compensation mechanisms in (Gd0. 2La0. 2Nd0. 2Sm0. 2Y0. 2) 1− xCaxFeO3. Int J Appl Ceram Technol 20(1):213–223

46. Gonzalez-Carrero S, Galian RE, Pérez-Prieto J (2016) Organic-inorganic and all-inorganic lead halide nanoparticles. Opt Express 24(2):A285–A301

47. Yin W-J et al (2019) Oxide perovskites, double perovskites and derivatives for electrocatalysis, photocatalysis, and photovoltaics. Energy Environ Sci 12(2):442–462

48. Zeng L et al (2020) In-situ modified the surface of Pt-doped perovskite catalyst for soot oxidation. J Hazard Mater 383:121210

49. Kalubarme RS et al (2014) LaNixCo1-xO3-δ perovskites as catalyst material for non-aqueous lithium-oxygen batteries. J Electrochem Soc 161(6):A880

50. Li M et al (2020) A CO2-tolerant perovskite oxide with high oxide ion and electronic conductivity. Adv Mater 32(4):1905200

51. Hussain MI et al (2020) Ab-initio prediction of the mechanical, magnetic and thermoelectric behaviour of perovskite oxides XGaO3 (X= Sc, Ti, Ag) using LDA+ U functional: for optoelectronic devices. J Mol Graph Model 99:107621

52. Chang H et al (2020) Effects of oxygen mobility in La–Fe-based perovskites on the catalytic activity and selectivity of methane oxidation. ACS Catal 10(6):3707–3719

53. Kumar S et al (2024) Surface modification of carbon nanofiber with C20H38O11 polymer by spun calcination method. J Inorg Organomet Polym Mater 34(1):336–345

54. Juarez-Perez EJ et al (2014) Photoinduced giant dielectric constant in lead halide perovskite solar cells. J Phys Chem Lett 5(13):2390–2394

55. Goel P et al (2021) Perovskite materials as superior and powerful platforms for energy conversion and storage applications. Nano Energ 80:105552

56. Hussain MI et al (2020) Investigations of structural, electronic and optical properties of TM-GaO3 (TM= Sc, Ti, Ag) perovskite oxides for optoelectronic applications: a first principles study. Mater Res Express 7(1):015906

57. Hussain I et al (2019) Structural, magnetic and magnetocaloric properties of double perovskites Ba2-xLaxFeMoO6. Solid State Sci 97:105991

58. Porta P et al (1999) Perovskite-type oxides: I. Structural, magnetic, and morphological properties of LaMn1− xCuxO3 and LaCo1− xCuxO3 solid solutions with large surface area. J Solid State Chem 146(2):291–304

59. Wang W et al (2019) Synthesis, morphology and electrochemical performances of perovskite-type oxide LaxSr1-xFeO3 nanofibers prepared by electrospinning. J Phys Chem Solids 124:144–150

60. Ichimura K, Inoue Y, Yasumori I (1992) Hydrogenation and hydrogenolysis of hydrocarbons on perovskite oxides. Catal Rev 34(4):301–320

61. Aftab S, Nawaz T, Tahir MB (2021) Recent development in shape memory based perovskite materials for energy conversion and storage applications. Int J Energy Res 45(15):20545–20558

62. Waleed A et al (2017) All inorganic cesium lead iodide perovskite nanowires with stabilized cubic phase at room temperature and nanowire array-based photodetectors. Nano Lett 17(8):4951–4957

63. Ye HY et al (2014) An above-room-temperature ferroelectric organo–metal halide perovskite:(3-pyrrolinium)(CdCl3). Angew Chem 126(42):11424–11429

64. Zhang X et al (2019) Controlled synthesis and photonics applications of metal halide perovskite nanowires. Small Methods 3(1):1800294

65. Zhu Z et al (2018) Metal halide perovskites: stability and sensing-ability. Journal of Materials Chemistry C 6(38):10121–10137

66. Xia Y et al (2009) Shape-controlled synthesis of metal nanocrystals: simple chemistry meets complex physics? Angew Chem Int Ed 48(1):60–103

67. Romero G, Moya SE (2012) Synthesis of organic nanoparticles. Frontiers of nanoscience. Elsevier, pp 115–141

68. Ahmed M (2020) Nanomaterial synthesis. Polymer science and nanotechnology. Elsevier, pp 361–399

69. Azharuddin M et al (2019) A repertoire of biomedical applications of noble metal nanoparticles. Chem Commun 55(49):6964–6996

70. Lal M et al (2018) Study of structural, electrical and magnetic properties of 1− x (Ba 0.96 Ca 0.04 TiO$_3$)− x (BiFeO$_3$) ceramics composites. J Mater Sci : Mater Electron 29:13984–14002

71. Sharma J, Kumar D, Sharma AK (2021) Structural and dielectric properties of pure potassium sodium niobate (KNN) lead free ceramics. Solid State Commun 334:114345

72. Kolahalam LA et al (2019) Review on nanomaterials: synthesis and applications. Mater Today: Proc 18:2182–2190

73. Wongpratat U, Maensiri S, Swatsitang E (2015) EXAFS study of cations distribution dependence of magnetic properties in Co1−xZnxFe2O4 nanoparticles prepared by hydrothermal method. Microelectron Eng 146:68–75

74. Li M et al (2017) Synthesis and characterization of nanosized MnZn ferrites via a modified hydrothermal method. J Magn Magn Mater 439:228–235

75. Obreja P et al (2019) Influence of surface substrates on the properties of ZnO nanowires synthesized by hydrothermal method. Appl Surf Sci 463:1117–1123

76. Wang T et al (2019) Hydrothermal preparation of Ag-TiO2-reduced graphene oxide ternary microspheres structure composite for enhancing photocatalytic activity. Physica E 112:128–136

77. Shandilya M, Rai R, Zeb A (2018) Structural and dielectric relaxor properties of Ba1-x Mg x TiO$_3$ ceramics prepared through a hydrothermal route. Adv Appl Ceram 117(5):255–263

78. Kaur GA et al (2022) Effect of addition of Ga$_2$O$_3$ on structural and morphological properties of Ba0. 85Ca0. 15Zr0. 10Ti0. 90O3 by sol-hydrothermal method. In: AIP conference proceedings, vol 2357. No 1. AIP Publishing

79. Kumar S et al (2022) Influence of Ga$_2$O$_3$ on structural and morphological properties of lead-free BCT at low temperature. In: AIP conference proceedings, vol 2357, No 1. AIP Publishing

80. Messing GL et al (2004) Templated grain growth of textured piezoelectric ceramics. Crit Rev Solid State Mater Sci 29(2):45–96

81. Mitsui T, Westphal WB (1961) Dielectric and X-ray studies of Ca x Ba 1–x Ti O 3 and Ca x Sr 1–x Ti O 3. Phys Rev 124(5):1354

82. Cheng X, Shen M (2007) Enhanced spontaneous polarization in Sr and Ca co-doped BaTiO3 ceramics. Solid State Commun 141(11):587–590

83. Kalyani AK et al (2014) Orthorhombic-tetragonal phase coexistence and enhanced piezo-response at room temperature in Zr, Sn, and Hf modified BaTiO3. Appl Phys Lett 104(25):252906

84. Kaur GA et al (2021) Structural and ferroelectric growth of Ba 0.85 Mg 0.15 TiO3–Ga$_2$O$_3$ ceramic through hydrothermal method. J Mater Sci : Mater Electron 32:23631–23644

85. Teraoka Y, Nobunaga T, Yamazoe N (1988) Effect of cation substitution on the oxygen semipermeability of perovskite-type oxides. Chem Lett 17(3):503–506

86. Shandilya M, Thakur S, Rai R (2019) Study of phase transitional behavior and electrical properties of relaxor Ba0. 85Ca0. 15Zr0. 05Ti0. 95O3 lead free ceramic. Ferroelectr Lett Sect 46(1–3):8–18

87. Müller KA (2010) Properties of perovskites and other oxides. World Scientific Publishing Company Pte Limited, Singapore

88. Shandilya M, Verma R (2021) Impedance modulated dielectric and magnetic properties of BCT-NF multiferroic composite. J Magnet Magn Mater 527:167782

89. Hao J et al (2019) Progress in high-strain perovskite piezoelectric ceramics. Mater Sci Eng R Rep 135:1–57

90. Jbaily A, Yeung RW (2015) Piezoelectric devices for ocean energy: a brief survey. J Ocean Eng Mar Energ 1:101–118

91. Quan ND et al (2014) Current development in lead-free Bi0. 5 (Na, K) 0.5 TiO$_3$-based piezoelectric materials. Adv Mater Sci Eng 20141:365391

92. Tao H, Wu J (2017) New poling method for piezoelectric ceramics. J Mater Chem C 5(7):1601–1606

93. Brown C et al (1962) Piezoelectric materials, a review of progress. IRE Trans Component Parts 9(4):193–211

94. Sodano HA, Inman DJ, Park G (2004) A review of power harvesting from vibration using piezoelectric materials. Shock and Vibration Digest 36(3):197–206

95. Shandilya M et al (2021) Heavy metal recovery from wastewater by using iron-based nanomaterials. 319–339

96. Lang SB (1999) The history of pyroelectricity: from ancient Greece to space missions. Ferroelectrics 230(1):99–108

97. He H et al (2020) Advances in lead-free pyroelectric materials: a comprehensive review. Journal of Mater Chem C 8(5):1494–1516

98. Cooper J (1962) A fast response total-radiation detector. Nature 194(4825):269–271

99. Chynoweth A (1956) Dynamic method for measuring the pyroelectric effect with special reference to barium titanate. J Appl Phys 27(1):78–84

100. Chynoweth A (1960) Pyroelectricity, internal domains, and interface charges in triglycine sulfate. Phys Rev 117(5):1235

101. Whatmore R, Osbond P, Shorrocks N (1987) Ferroelectric materials for thermal IR detectors. Ferroelectrics 76(1):351–367

102. Li X et al (2013) Pyroelectric and electrocaloric materials. J Mater Chem C 1(1):23–37

103. Lang SB (2005) Pyroelectricity: from ancient curiosity to modern imaging tool. Phys Today 58(8):31–36

104. Wang ZL et al (2012) Progress in nanogenerators for portable electronics. Mater Today 15(12):532–543

105. Bowen CR et al (2014) Pyroelectric materials and devices for energy harvesting applications. Energ Environ Sci 7(12):3836–3856

106. Yi Z et al (2019) Will organic–inorganic hybrid halide lead perovskites be eliminated from optoelectronic applications? Nanoscale Adv 1(4):1276–1289

107. López-Juárez R et al (2011) Ferroelectric domain structure of lead-free potassium-sodium niobate ceramics. J Eur Ceram Soc 31(9):1861–1864

108. Smith MB et al (2008) Crystal structure and the paraelectric-to-ferroelectric phase transition of nanoscale BaTiO3. J Am Chem Soc 130(22):6955–6963

109. Cohen RE (1992) Origin of ferroelectricity in perovskite oxides. Nature 358(6382):136–138

110. Assirey EAR (2019) Perovskite synthesis, properties and their related biochemical and industrial application. Saudi Pharml J 27(6):817–829

111. Vasudevan RK et al (2017) Ferroelectric or non-ferroelectric: why so many materials exhibit "ferroelectricity" on the nanoscale. Appl Phys Rev 4(2):021302

112. Kumar S et al (2022) Effect of excessive amount of (Na, K) ion ratio on structural, optical and electrical properties of K0. 5Na0. 5NbO$_3$ ceramics prepared by solid-state route. Bull Mater Sci 45(1):30

113. Luedtke W, Gao J, Landman U (2011) Dielectric nanodroplets: structure, stability, thermodynamics, shape transitions and electrocrystallization in applied electric fields. J Phys Chem C 115(42):20343–20358

114. Haertling GH (1999) Ferroelectric ceramics: history and technology. J Am Ceram Soc 82(4):797–818

115. Jin L, Li F, Zhang S (2014) Decoding the fingerprint of ferroelectric loops: comprehension of the material properties and structures. J Am Ceram Soc 97(1):1–27

116. Shrout TR, Zhang SJ (2007) Lead-free piezoelectric ceramics: alternatives for PZT? J Electroceram 19:113–126

117. Li J et al (2005) Domain switching in polycrystalline ferroelectric ceramics. Nat Mater 4(10):776–781

118. Ortega-San-Martin L (2020) Introduction to perovskites: a historical perspective. In: Revolution of perovskite: synthesis, properties and applications, pp 1–41

119. Von Hippel A et al (1946) High dielectric constant ceramics. Ind Eng Chem 38(11):1097–1109

120. Pattanayak DK et al (2023) Electronic applications of perovskite. In: Perovskite metal oxides. Elsevier, pp 315–339

121. Randall CA et al (1990) Classification and consequences of complex lead perovskite ferroelectrics with regard to B-site cation order. J Mater Res 5(4):829–834

122. Kittel C, McEuen P, McEuen P (1996) Introduction to solid state physics, vol 8. Wiley, New York

123. Bednorz JG, Müller KA (1986) Possible high T c superconductivity in the Ba− La− Cu− O system. Zeitschrift für Physik B Condensed Matter 64(2):189–193

124. Babu TN, Fish DJ, Greaves C (1991) Synthesis, structure and electrical properties of Sr 2 CuO 2 (CO 3), an oxide carbonate related to perovskite. J Mater Chem 1(4):677–679

125. Özkurt B (2020) Effect of annealing conditions on the superconducting properties of nano-sized metallic au-added Bi1. 8Sr2Au0. 2Ca1. 1Cu2. 1O y (Bi-2212) ceramics. J Maters Sci : Mater Electron 31(14):11448–11456

126. Manser JS, Christians JA, Kamat PV (2016) Intriguing optoelectronic properties of metal halide perovskites. Chem Rev 116(21):12956–13008

127. Sleight A, Gillson J, Bierstedt P (1993) High-temperature superconductivity in the BaPb1− xBixO3 system. Solid State Commun 88(11–12):841–842

128. Kumar S et al (2024) Interface engineering of composite systems: focusing on the compatibility of reduced graphene oxide and Bi0. 8La0. 1Ba0. 1Fe0. 9Ti0. 1O3 hybrid systems. Mater Today Sustain 27:100813

129. Cox D, Sleight A (1976) Crystal structure of Ba2Bi3+ Bi5+ O6. Solid State Commun 19(10):969–973

130. Cox D, Sleight A (1979) Mixed-valent Ba2Bi3+ Bi5+ O6: structure and properties vs temperature. Acta Crystallogr Sect B: Struct Crystallogr Cryst Chem 35(1):1–10

131. Thornton G, Jacobson A (1978) A neutron diffraction determination of the structures of Ba2SbVBiIIIO6 and Ba2BiVBiIIIO6. Acta Crystallogr Sect B: Struct Crystallogr Cryst Chem 34(2):351–354

132. Harabor A et al (2023) Structural, thermal and superconducting properties of Ag$_2$O-doped YBa$_2$Cu$_3$O$_7$-x composite materials. Ceram Int 49(9):14904–14916

133. Muhammad Y et al (2022) Impact of high pelletize pressure on superconducting properties of (Cu) x/CuTl-1223 composites. J Supercond Nov Magn 35(3):669–678

134. Muhammad Y et al (2023) Comparative investigation of low and high pelletize pressure for (ag) x/CuTl-1223 nanoparticles-superconductor composites. Phys Scr 98(12):125967

135. Kim M et al (2021) Mixed valence and superconductivity in perovskite antimonates. Chem Mater 33(17):6787–6793

136. Cantaluppi A et al (2018) Pressure tuning of light-induced superconductivity in K3C60. Nat Phys 14(8):837–841

137. Tütüncü HM, Srivastava GP (2012) Phonons and superconductivity in the cubic perovskite Cr3RhN. J Appl Phys 112:9

138. Zheng JP et al (1991) Noise measurement of YBa$_2$Cu$_3$O$_7$− x and Ti$_2$Ba$_2$Ca$_2$Cu$_3$O10− x thin films. J Appl Phys 69(1):553–555

139. Mao ZQ et al (2003) Experimental determination of superconducting parameters for the intermetallic perovskite superconductor MgCNi$_3$. Phys Rev B 67(9):094502

140. Chang MC et al (2001) The effect of ball-milling solvent on the decomposition properties of Ba (Pb1−xBix) O3. Mater Chem Phys 69(1–3):226–229

141. Tarascon J-M et al (1987) Superconductivity at 40 K in the oxygen-defect perovskites La2-x Sr x CuO4-y. Science 235(4794):1373–1376

142. Takei H et al (1986) Magnetic and superconducting properties of the cubic perovskite YRh3B. J Less Common Met 125:233–237

143. Cheng Z et al (2019) Strain tuning effects in perovskites. Nanoscale ferroelectric-multiferroic materials for energy harvesting applications. Elsevier, pp 23–39

144. Ibn-Mohammed T et al (2017) Perovskite solar cells: an integrated hybrid lifecycle assessment and review in comparison with other photovoltaic technologies. Renew Sustain Energy Rev 80:1321–1344

145. Xiao JW et al (2017) The emergence of the mixed perovskites and their applications as solar cells. Adv Energy Mater 7(20):1700491

146. Jung HS, Park N-G (2015) Perovskite solar cells: from materials to devices. Small 11(1):10–25

147. Kojima A et al (2009) Organometal halide perovskites as visible-light sensitizers for photovoltaic cells. J Am Chem Soc 131(17):6050–6051

148. Kazmerski L (2012) Best research cell efficiencies chart. National Renewable Energy Laboratory (NREL)

149. Cann O (2016) These are the top 10 emerging technologies of 2016. in World economic forum

150. Dong Q et al (2015) Electron-hole diffusion lengths> 175 μm in solution-grown CH3NH3PbI3 single crystals. Science 347(6225):967–970

151. Liu M, Johnston MB, Snaith HJ (2013) Efficient planar heterojunction perovskite solar cells by vapour deposition. Nature 501(7467):395–398

152. Stranks SD et al (2013) Electron-hole diffusion lengths exceeding 1 micrometer in an organometal trihalide perovskite absorber. Science 342(6156):341–344

153. Xing G et al (2013) Long-range balanced electron-and hole-transport lengths in organic-inorganic CH3NH3PbI3. Science 342(6156):344–347

154. Mahmood K, Sarwar S, Mehran MT (2017) Current status of electron transport layers in perovskite solar cells: materials and properties. RSC Adv 7(28):17044–17062

155. Liu D, Gangishetty MK, Kelly TL (2014) Effect of CH 3 NH 3 PbI 3 thickness on device efficiency in planar heterojunction perovskite solar cells. J Mater Chem A 2(46):19873–19881

156. Kim Y et al (1997) SiO$_2$ colloidal effects on the twisted intramolecular charge transfer of pN, Ndimethylaminobenzoic acid in acetonitrile. Chem Phys Lett 264(6):673–679

157. Zhou Y et al (2022) Advances and challenges in understanding the microscopic structure–property–performance relationship in perovskite solar cells. Nat Energy 7(9):794–807

158. Hanif MB et al (2022) Recent progress of perovskite-based electrolyte materials for solid oxide fuel cells and performance

optimizing strategies for energy storage applications. Mater Res Bull 146:111612

159. Sikstrom D et al (2023) Perovskite-type Nd0. 75Ba0. 25Co0. 8Fe0. 2O3-δ cathode for intermediate temperature solid oxide fuel cells. Ionics 29(4):1507–1514

160. Yatoo MA et al (2023) Solid-oxide fuel cells: a critical review of materials for cell components. MRS Commun 13(3):378–384

161. Dwivedi S (2020) Solid oxide fuel cell: materials for anode, cathode and electrolyte. Int J Hydrogen Energy 45(44):23988–24013

162. Kaur P, Singh K (2020) Review of perovskite-structure related cathode materials for solid oxide fuel cells. Ceram Int 46(5):5521–5535

163. Wang R (2023) Review of materials for solid oxide fuel cell. Highlights Sci Eng Technol 46:176–180

164. Xiao G et al (2012) Synthesis and characterization of Mo-doped SrFeO3− δ as cathode materials for solid oxide fuel cells. J Power Sources 202:63–69

165. Fu D, Jin F, He T (2016) A-site calcium-doped Pr1− xCaxBaCo2O5+δ double perovskites as cathodes for intermediate-temperature solid oxide fuel cells. J Power Sources 313:134–141

166. Olszewska A et al (2019) Mn-rich SmBaCo0. 5Mn1. 5O5+ δ double perovskite cathode material for SOFCs. Int J Hydrog Energy 44(50):27587–27599

167. Zhu X et al (2019) Perovskite-type Nd0. 5Sr0. 5Co0. 5Fe0. 5O3-δ as a novel cathode material for intermediate-temperate solid oxide fuel cell. J Alloys Compd 802:415–421

168. Li L et al (2015) Cobalt-free double perovskite cathode GdBaFeNiO5+ δ and electrochemical performance improvement by Ce0. 8Sm0. 2O1. 9 impregnation for intermediate-temperature solid oxide fuel cells. Electrochim Acta 182:682–692

169. Xu X et al (2019) Impressive performance of proton-conducting solid oxide fuel cells using a first-generation cathode with tailored cations. J Mater Chem A 7(32):18792–18798

170. Mao X, Yu T, Ma G (2015) Performance of cobalt-free double-perovskite NdBaFe2− xMnxO5+ δ cathode materials for proton-conducting IT-SOFC. J Alloy Compd 637:286–290

171. Xia W et al (2020) Evaluation of calcium codoping in double perovskite PrBaCo2O5+ δ as cathode material for IT-SOFCs. Electrochim Acta 364:137274

172. Jin F et al (2013) Characterization and evaluation of double perovskites LnBaCoFeO5+ δ (Ln= Pr and Nd) as intermediate-temperature solid oxide fuel cell cathodes. J Power Sources 243:10–18

173. Jin F, Li L, He T (2015) NdBaCo2/3Fe2/3Cu2/3O5+ δ double perovskite as a novel cathode material for CeO2-and LaGaO3-based solid oxide fuel cells. J Power Sources 273:591–599

174. Lü S et al (2014) Performance of double-perovskite YBa0. 5Sr0. 5Co1. 4Cu0. 6O5+ δ as cathode material for intermediate-temperature solid oxide fuel cells. Ceram Int 40(9):14919–14925

175. Hou M et al (2014) Investigation into the effect of molybdenum-site substitution on the performance of Sr2Fe1. 5Mo0. 5O6− δ for intermediate temperature solid oxide fuel cells. J Power Sources 272:759–765

176. Hu Y et al (2013) Synthesis, physical–chemical characterization and electrochemical performance of GdBaCo2− xNixO5+ δ (x= 0–0.8) as cathode materials for IT-SOFC application. J Power Sources 242:50–56

177. Gu H et al (2021) SrCo0. 8Ti0. 1Ta0. 1O3-δ perovskite: a new highly active and durable cathode material for intermediate-temperature solid oxide fuel cells. Compos Part B 213:108726

178. Gou Y et al (2021) Pr-doping motivating the phase transformation of the BaFeO3-δ perovskite as a high-performance solid oxide fuel cell cathode. ACS Appl Mater Interfaces 13(17):20174–20184

179. Zainon AN et al (2023) Challenges in using perovskite-based anode materials for solid oxide fuel cells with various fuels: a review. Int J Hydrog Energy

180. Chen S et al (2023) Tailored double perovskite with boosted oxygen reduction kinetics and CO2 durability for solid oxide fuel cells. ACS Sustain Chem Eng 11(35):13198–13208

181. Zhang B et al (2023) Cobalt-free double perovskite oxide as a promising cathode for solid oxide fuel cells. ACS Appl Mater Interfaces 15(6):8253–8262

182. Zhang L et al (2010) Double-perovskites A2FeMoO6− δ (A= Ca, Sr, Ba) as anodes for solid oxide fuel cells. J Power Sources 195(19):6356–6366

183. Li W et al (2015) Evaluation of double perovskite Sr2FeTiO6− δ as potential cathode or anode materials for intermediate-temperature solid oxide fuel cells. Ceram Int 41(9):12393–12400

184. Song Y et al (2014) Effect of cobalt-substitution Sr2Fe1. 5-xCoxMo0. 5O6-δ for intermediate temperature symmetrical solid oxide fuel cells fed with H2-H2S. Electrochim Acta 139:13–20

185. Martínez-Coronado R et al (2013) Reversible oxygen removal and uptake in the La2ZnMnO6 double perovskite: performance in symmetrical SOFC cells. Solid State Sci 18:64–70

186. Ding H et al (2016) A redox-stable direct-methane solid oxide fuel cell (SOFC) with Sr2FeNb0.2Mo0. 8O6− δ double perovskite as anode material. J Power Sources 327:573–579

187. Sun Y-F et al (2016) Molybdenum doped Pr0. 5Ba0. 5MnO3− δ (Mo-PBMO) double perovskite as a potential solid oxide fuel cell anode material. J Power Sources 301:237–241

188. Cascos V et al (2017) Design of new Ga-doped SrMoO3 perovskites performing as anode materials in SOFC. Renew Energy 111:476–483

189. Qi H et al (2019) Reduced thermal expansion and enhanced redox reversibility of La0. 5Sr1. 5Fe1. 5Mo0. 5O6− δ anode material for solid oxide fuel cells. ACS Appl Energy Mater 2(6):4244–4254

190. Sengodan S et al (2015) Layered oxygen-deficient double perovskite as an efficient and stable anode for direct hydrocarbon solid oxide fuel cells. Nat Mater 14(2):205–209

191. Cascos V, Alonso JA, Fernández-Díaz MT (2016) Novel Mg-doped SrMoO3 perovskites designed as anode materials for solid oxide fuel cells. Materials 9(7):588

192. Dimos D, Mueller C (1998) Perovskite thin films for high-frequency capacitor applications. Annu Rev Mater Sci 28(1):397–419

193. Shandilya M, Kaur GA, Rai R (2021) Low temperature consequence on structural and impedance properties of BST ceramics via sol-hydrothermal method. Mater Chem Phys 263:124422

194. Peng B et al (2015) Giant electric energy density in epitaxial lead-free thin films with coexistence of ferroelectrics and antiferroelectrics. Adv Electron Mater 1(5):1500052

195. Chu B et al (2006) A dielectric polymer with high electric energy density and fast discharge speed. Science 313(5785):334–336

196. Yin J et al (2018) Ultrahigh energy-storage potential under low electric field in bismuth sodium titanate-based perovskite ferroelectrics. J Mater Chem A 6(21):9823–9832

197. Yang L et al (2019) Perovskite lead-free dielectrics for energy storage applications. Prog Mater Sci 102:72–108

198. Zou K et al (2019) Recent advances in lead-free dielectric materials for energy storage. Mater Res Bull 113:190–201

199. Kwon D-K, Lee MH (2012) Temperature-stable high-energy-density capacitors using complex perovskite thin films. IEEE Trans Ultrason Ferroelectr Freq Control 59(9):1894–1899

200. Hou C et al (2017) Ultrahigh energy density in SrTiO3 film capacitors. ACS Appl Mater Interfaces 9(24):20484–20490

201. Chen P et al (2018) Great enhancement of energy storage density and power density in BNBT/x BFO multilayer thin film hetero-structures. Inorg Chem Frontiers 5(9):2300–2305

202. Chen P et al (2017) Enhanced dielectric and energy-storage properties in BiFeO3-modified Bi0. 5 (Na0. 8K0. 2) 0.5 TiO$_3$ thin films. Ceram Int 43(16):13371–13376

203. Chen P et al (2018) High recoverable energy storage density in (1-x) Bi0. 5 (Na0. 8K0. 2) 0.5 TiO3-xSrZrO$_3$ thin films prepared by a sol-gel method. J Eur Ceram Soc 38(14):4640–4645

204. Xie J et al (2019) A novel lead-free bismuth magnesium titanate thin films for energy storage applications. J Am Ceram Soc 102(7):3819–3822

205. Li Z et al (2019) Novel BiAlO3 dielectric thin films with high energy density. Ceram Int 45(17):22523–22527

206. Zhao Y, Hao X, Li M (2014) Dielectric properties and energy-storage performance of (Na0. 5Bi0. 5) TiO$_3$ thick films. J Alloys Compd 601:112–115

207. Diao C et al (2019) Significantly improved energy storage properties of sol-gel derived Mn-modified SrTiO3 thin films. Ceram Int 45(9):11784–11791

208. Won SS et al (2017) BiFeO3-doped (K0. 5, Na0. 5)(Mn0. 005, Nb0. 995) O3 ferroelectric thin film capacitors for high energy density storage applications. Appl Phys Lett 110:152901

209. Tang Z et al (2018) High energy-storage density of lead-free BiFeO$_3$ doped Na0. 5Bi0. 5TiO3-BaTiO$_3$ thin film capacitor with good temperature stability. J Alloys Compd 757:169–176

210. Xing G et al (2014) Low-temperature solution-processed wavelength-tunable perovskites for lasing. Nat Mater 13(5):476

211. Stranks SD et al (2015) Enhanced amplified spontaneous emission in perovskites using a flexible cholesteric liquid crystal reflector. Nano Lett 15(8):4935–4941

212. Saliba M et al (2016) Structured organic–inorganic perovskite toward a distributed feedback laser. Adv Mater 28(5):923–929

213. Dhanker R et al (2014) Random lasing in organo-lead halide perovskite microcrystal networks. Appl Phys Lett 105(15):151112

214. Yakunin S et al (2015) Low-threshold amplified spontaneous emission and lasing from colloidal nanocrystals of caesium lead halide perovskites. Nat Commun 6:8056

215. Chang T-C et al (2016) Resistance random access memory. Mater Today 19(5):254–264

216. Chappert C, Fert A, Van Dau FN (2007) The emergence of spin electronics in data storage. Nat Mater 6(11):813–823

217. Kao KF et al (2009) Ga2Te3Sb5—a candidate for fast and ultralong retention phase-change memory. Adv Mater 21(17):1695–1699

218. Han JS et al (2019) Lead-free all-inorganic cesium tin iodide perovskite for filamentary and interface-type resistive switching toward environment-friendly and temperature-tolerant nonvolatile memories. ACS Appl Mater Interfaces 11(8):8155–8163

219. Cheng X-F et al (2017) Poly (3, 4-ethylenedioxythiophene)–poly (styrenesulfonate) interlayer insertion enables organic quaternary memory. ACS Appl Mater Interfaces 9(33):27847–27852

220. Liu SJ et al (2012) Single polymer-based ternary electronic memory material and device. Adv Mater 24(21):2901–2905

221. Hu C et al (2014) Highly controllable and stable quantized conductance and resistive switching mechanism in single-crystal TiO2 resistive memory on silicon. Nano Lett 14(8):4360–4367

222. Nili H et al (2014) Nanoscale resistive switching in amorphous perovskite oxide (a-SrTiO3) memristors. Adv Func Mater 24(43):6741–6750

223. Ercan E et al (2018) Influence of polymeric electrets on the performance of derived hybrid perovskite-based photo-memory devices. Nanoscale 10(39):18869–18877

224. Xiao Z, Huang J (2016) Energy-efficient hybrid perovskite memristors and synaptic devices. Advanced Electronic Materials 2(7):1600100

225. Stoumpos CC, Malliakas CD, Kanatzidis MG (2013) Semiconducting tin and lead iodide perovskites with organic cations: phase transitions, high mobilities, and near-infrared photoluminescent properties. Inorg Chem 52(15):9019–9038

226. Tian W, Zhou H, Li L (2017) Hybrid organic–inorganic perovskite photodetectors. Small 13(41):1702107

227. Chen JY et al (2017) Nonvolatile perovskite-based photomemory with a multilevel memory behavior. Adv Mater 29(33):1702217

228. Hwang B, Lee J-S (2018) Lead-free, air-stable hybrid organic–inorganic perovskite resistive switching memory with ultrafast switching and multilevel data storage. Nanoscale 10(18):8578–8584

229. Wong H-SP et al (2012) Metal–oxide RRAM. Proc IEEE 100(6):1951–1970

230. Liu C-Y, Tseng T-Y (2007) Resistance switching properties of sol–gel derived SrZrO3 based memory thin films. J Phys D Appl Phys 40(7):2157

231. Lin M-H et al (2011) High device yield of resistive switching characteristics in oxygen-annealed $\hbox{SrZrO}_3$ memory devices. IEEE Trans Electron Devices 58(4):1182–1188

232. Lin M-H et al (2010) Resistive switching characteristics and mechanisms of Pt-embedded SrZrO 3 memory devices. J Appl Phys 107(12):124117

233. Lin M-H et al (2010) High-speed and localized resistive switching characteristics of double-layer SrZrO3 memory devices. J Phys D Appl Phys 43(29):295404

234. Lin C-C et al (2006) Resistive switching mechanisms of V-doped hbox-SrZrO_3 memory films. IEEE Electron Device Lett 27(9):725–727

235. Liu C-Y et al (2005) Bistable resistive switching of a sputter-deposited Cr-doped SrZrO/sub 3/memory film. IEEE Electron Device Lett 26(6):351–353

236. Sze S (2006) Physics of semiconductor devices 2nd edition a Wiley inter-science John Wiley and Sons, New York. https://doi.org/10.1002/9780470068328.ch1